FACULTY
OF SCIENCE

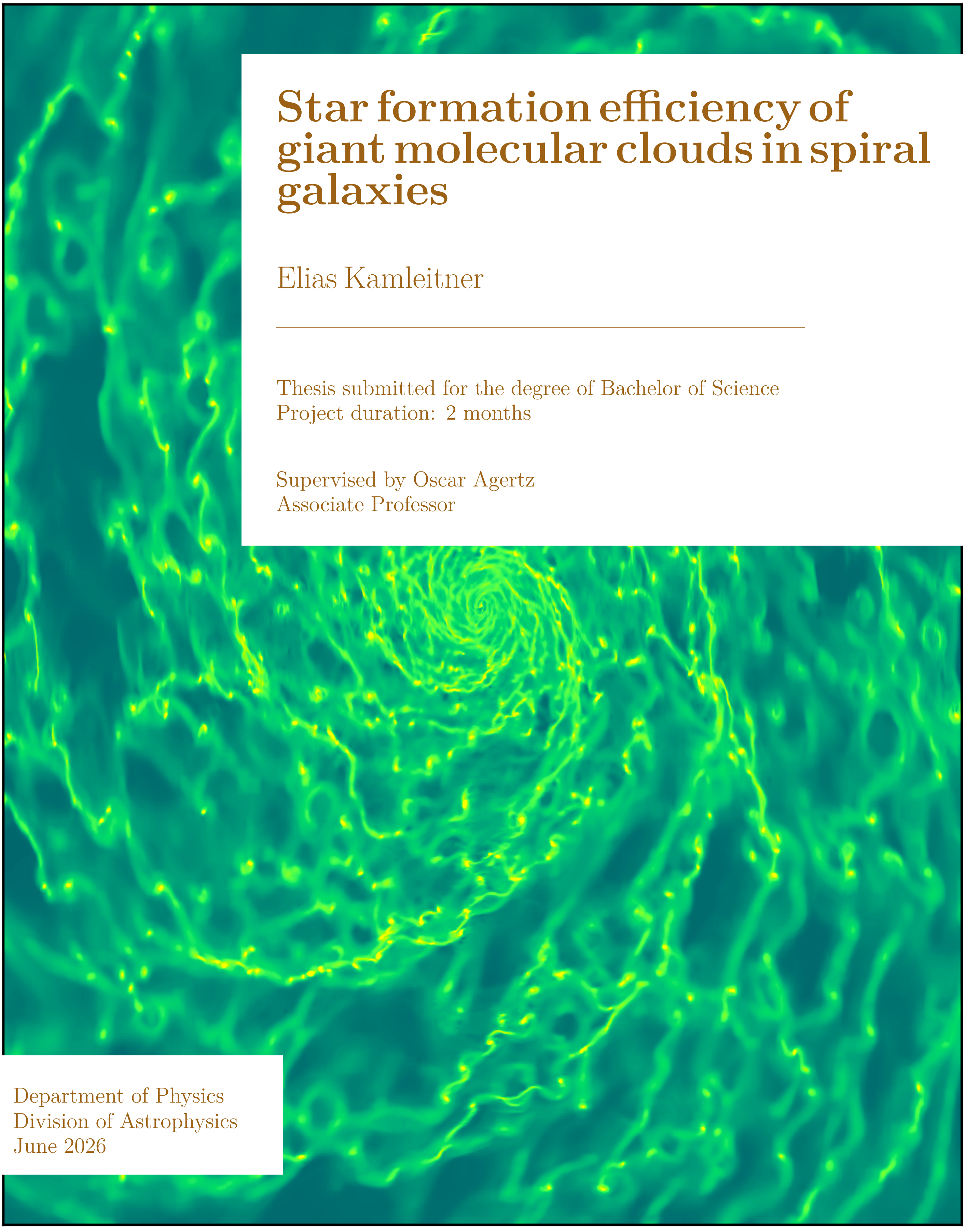

Star formation efficiency of giant molecular clouds in spiral galaxies

Elias Kamleitner

Thesis submitted for the degree of Bachelor of Science
Project duration: 2 months

Supervised by Oscar Agertz
Associate Professor

Department of Physics
Division of Astrophysics
June 2026

2026–EXA262
FYSK04 2026-06-10

Degree project of 15 higher education credits
June 2026

Supervisor: Oscar Agertz

Division of Astrophysics
Department of Physics
Box 118
SE-221 00 Lund
Sweden

Popular Description

The stars you see in the night sky were once part of a cold cloud of gas, but exactly how these clouds collapse to form stars is an open question in astrophysics. Stars are one of the key players in galactic evolution. Their formation and evolution are what drive the development and structure of galaxies. By converting interstellar gas into stellar cores, they ignite nuclear burning at their cores, creating new elements and producing immense amounts of power. They disperse the new material and energy into their surroundings through supernovae, one of the most energetic events in our universe. This changes their surroundings by blowing gas away, heating dust grains and ionising atoms around them.

Because stars influence their surroundings so strongly, it is a key interest to understand how stars form and how efficiently they do so. Current theories and observations agree that stars form in clouds of interstellar molecular gas. However, the underlying physics of how these stars form and the influence of cloud properties are not well understood. Most models assume that stars are born in the collapse of particularly dense regions of the cloud. This happens in both the centre of the cloud and in shock fronts caused by turbulent gas that travels faster than the local speed of sound. These shock fronts are similar to what happens when a plane breaches the sound barrier.

Instead of waiting millions of years to observe how stars form, this work investigates simulations of virtual galaxies. By starting all simulations off the same way and letting them develop over a span of several hundred million years, we can look at the differences caused by different star formation models. To be able to compare the simulations with large-scale surveys of galaxies outside our own, we observe our simulations as if we were real astronomers looking through a telescope. In this way, we can calculate several key properties of the clouds and their efficiency at forming stars. This then allows us to examine the different models and determine which families of models best reproduce the observed data.

The main interest of the thesis is to figure out which models match the observed fraction of gas that gets turned into stars during the collapse of a cloud. We also investigate how the effects of newly formed stars influence the birth of future stars.

We find that different models can produce very different outcomes that completely change how galaxies look. Some produce clumpy gas while others create cloudless, dispersed galaxies. Compared to observational data, the results show that the observations are best matched with models that are internally converting only very little of their gas into stars. We also observe that while the effects of newly formed stars have a large impact on the general structure of galaxies, they do not influence individual clouds as much.

This work indicates which models accurately describe what is happening in gas clouds in our universe and how they form stars. The results allow us to choose better models when simulating galaxies, putting us one step closer to having fully accurate simulations of the universe around us. Helping us to understand both how our galaxy formed and how it will develop in the future.

Abstract

Context. Star formation (SF) remains an incompletely understood concept essential to many fields of astrophysics. Observations show that star-forming giant molecular clouds (GMCs) form around 1 per cent or less stars per free-fall time. This trend is observed over all nearby galaxies observed to date by the The Physics at High Angular resolution in Nearby GalaxieS ALMA Survey (PHANGS-ALMA) collaboration. This makes SF a highly inefficient process. It is not known whether this is an effect of stellar feedback processes that regulate SF, or if clouds are intrinsically inefficient at converting gas into stars. *Aims.* This thesis aims to analyse a suite of simulations implementing different SF models to determine which model types can reproduce observed star formation efficiencys (SFEs). We further investigate the effects of stellar feedback, specifically the extent to which it can regulate SFE. *Methods.* Isolated Milky Way mass galaxy simulations are compared to data from the PHANGS-ALMA collaboration. The simulations are mock observed to enable a direct comparison with the analysis of Leroy et al. (2025). *Results.* The results show that intrinsically inefficient models are better at reproducing observational data. Feedback has a small effect on local properties with a larger influence on global parameters, and even low complexity models, such as fixed input efficiencies, can match the low observed efficiencies with the correct input efficiency. In contrast, models with high intrinsic SFEs and strong feedback, which are often employed in cosmological simulations, are shown to fail at reproducing observed cloud-scale trends and SFEs. *Conclusions.* The findings give an indication of which models are reasonable at matching observed data and what parameters are important to determine SFEs. These findings indicate which models best reflect observational data and how feedback regulates properties. The results provide guidance in selecting and calibrating SF models for future galaxy-scale simulations.

Contents

List of Abbreviations

AMR	adaptive mesh refinement. 4, 7, 9
decalibrated FK model	Decalibrated model for star formation efficiency following Kretschmer & Teyssier (2020).. 6, 13, 15–19, 25, 28, 31
eff001 model	Model for star formation efficiency with a fixed input efficiency of 1%. 13–15, 18–22, 24, 25
eff01 model	Model for star formation efficiency with a fixed input efficiency of 10%. 13, 30
eff1 model	Model for star formation efficiency with a fixed input efficiency of 100%. 13, 15, 20, 21, 30, 32
FK model	Model for star formation efficiency using the multi free-fall hydrodynamic KM model from Federrath & Klessen (2012) .. 5, 6, 16–19, 28, 31
GMC	giant molecular cloud. ii, 1, 3, 4, 18, 24, 25
IMF	initial mass function. 9
ISM	interstellar medium. 4, 6, 9
PHANGS-ALMA	The Physics at High Angular resolution in Nearby GalaxieS ALMA Survey. ii, 1, 8, 15, 18, 24, 25
PN model	Simple model for star formation following Padoan et al. (2012).. 4, 5, 15, 16, 19, 24, 25, 32
RT	radiative transfer. 9, 21, 22, 32
SF	star formation. ii, 1–4, 6, 8, 10, 13–15, 17–19, 21–25
SFE	star formation efficiency. ii, 1, 2, 4, 6, 9, 15, 17, 19, 21–23, 25
SFR	star formation rate. 1, 3, 10, 14, 15, 24
SN	supernova. 4, 6, 9, 13, 14, 20, 21
SPH	smoothed particle hydrodynamics. 6

Chapter 1

Introduction

Spiral galaxies such as our Milky Way undergo star formation (SF). Most of the newly formed stellar mass is created in so-called giant molecular clouds (GMCs) (Myers et al., 1986; Grisdale et al., 2019). Newly formed young stars include massive stars that significantly shape the galactic environment around them, as explained in more detail at the end of Section 2.1. It is therefore imperative to understand how stars form to be able to explain the evolution of galaxies. However, the process behind SF is not yet well understood, with several key properties unexplained. At the moment, it is unclear if models can produce star formation efficiency (SFE) at local scales. Many studies on SF investigated global parameters such as the Kennicutt-Schmidt relation (Kennicutt, 1998) and the stellar mass to halo mass relation (Moster et al., 2013; Behroozi et al., 2013). In literature, different quantities are defined as a measure of SFE. The Kennicutt-Schmidt relation, relating gas density to star formation rate (SFR) density, gives the depletion time, measuring the speed at which stars are formed, while the stellar mass to halo mass relation gives the total fraction of gas converted into stars. The SFE investigated in this work is the efficiency per free-fall time of a cloud. This value is independent of the lifetime of the cloud and is a measure of the fraction of gas converted into stars during the collapse of the cloud. This is different from the total SFE of a cloud, which measures the total mass of a cloud that was converted into stars.

The most extensive observations of star formation at a local scale are from the The Physics at High Angular resolution in Nearby GalaxieS ALMA Survey (PHANGS-ALMA). Leroy et al. (2025) investigated SFE in several galaxies outside the Milky Way in this survey, finding a median SFE per free-fall time of around 0.4%. This is somewhat surprisingly low, as one would expect a collapsing cloud to convert most gas into stars. The low efficiencies indicate that internal properties such as turbulence and feedback regulate this. They further discovered a weak anti-correlation between the gravitational boundness of a cloud and its SFE. This is in opposition to the theoretical understanding that bound clouds form stars more efficiently (Krumholz & McKee, 2005), expecting a correlation. Inferring SFEs from observation is complex, as the observed state of a cloud with young stars does not reflect the state of the clouds when the stars were formed. There is a time lag of a few Myrs, the time it takes from SF to the observation of the stars. Analytical theories provide the SFE at star formation while observations detect SFE at a later date. The arising discrepancies are discussed in the results below.

It is, therefore, of ongoing interest to find computational models that can match the observations and give us a greater understanding of the processes involved in SF. Models that have been developed differ in their approaches and what cloud properties they take into account (Federrath & Klessen, 2012; Padoan et al., 2012; Kretschmer & Teyssier, 2020), some of these models are outlined in detail in Section 2.2.

The work carried out for this thesis aims to investigate which computational models can match the cloud-scale observations by Leroy et al. (2025). The main interest is to see if there are models that can produce low efficiencies and replicate the observed correlation. Further investigations are done to see if these models keep the cloud properties reasonable and if there are modifications that can be done to the simulations, such as changing the feedback strength, to recover observed values. This will give insight into which model families, models that share a similar theoretical basis, better match the observations and if there are models that cannot be brought into agreement with the observational data.

The models are tested on purely hydrodynamical simulations of isolated galaxies; this means magnetic effects and disturbances by neighbouring galaxies or satellites will not be taken into account. Furthermore, the gas in the galaxy is not chemically traced in the simulations, introducing the need to estimate the distribution of molecular hydrogen, important in the calculations of SFE. These are assumptions and simplifications introduced due to the limited scope of the study. The sensitivity to some of those constraints, in particular, the selection of molecular hydrogen, is explored in Section 4.8. However, following the observational methods outlined by Leroy et al. (2025) closely, this work still provides a detailed investigation that is more suitable for direct comparison than previous simulations, where gas was modelled in a box.

This work is organised as follows: in Chapter 2, a theoretical background of SF is presented. Section 2.2 discusses the investigated models. Chapter 3 details the methodology behind this work. Chapter 4 presents the key results obtained along with a discussion and investigation of the limitations. Finally, in Chapter 5, an outlook is presented detailing future steps.

Chapter 2

Theory

2.1 Star formation in general

Stars form out of molecular hydrogen in GMCs. These are over-dense regions of molecular gas that interact gravitationally. Stars form when regions in these clouds become dense enough to collapse. This happens both in strongly gravitationally bound clouds and in shock fronts created by the supersonic movements of the gas within the clouds. The strength of shock fronts is quantified by the Mach number of the gas $\mathcal{M}_{\mathrm{s}} = \sigma_{\mathrm{v}}/c_{\mathrm{s}}$, measuring the ratio of the gas velocity dispersion σ_{v} and the speed of sound c_{s}. A higher $\mathcal{M}_{\mathrm{s}}$ corresponds to more and stronger shock fronts leading to a higher SFR (Federrath & Klessen, 2012). The SFR of the clouds is measured by the amount of molecular gas that is converted into stellar mass per unit time. Another measurement of SF is the depletion time

$$\tau_{\mathrm{dep}} = \frac{\Sigma_{\mathrm{mol}}}{\Sigma_{\mathrm{SFR}}}, \tag{2.1}$$

measuring how long it takes for a molecular cloud to be fully turned into stars. Here Σ_{mol} is the molecular surface density and Σ_{SFR} is the SFR per unit area. To compare SFRs, the star formation efficiency per free fall time ϵ_{ff}, a dimensionless quantity measuring the molecular mass fraction turned into stars per free fall time τ_{ff} (defined below in Equation 2.3), is often used

$$\epsilon_{\mathrm{ff}} = \frac{\tau_{\mathrm{ff}}}{\tau_{\mathrm{dep}}}. \tag{2.2}$$

This efficiency is expected to depend on the properties of clouds, which vary from cloud to cloud, responding to the galactic environment surrounding them (Leroy et al., 2025). To compare and classify the properties of the clouds, it is assumed that they are spherical and uniform in density. This, while an unrealistic assumption, is needed for analytical treatment and calculations of cloud-based properties (Federrath & Klessen, 2012). The free-fall time, the characteristic time it takes for clouds to collapse under their own gravity, is then given by

$$\tau_{\mathrm{ff}} = \sqrt{\frac{3\pi}{32G\rho_{\mathrm{mol}}}}, \tag{2.3}$$

where ρ_{mol} is the density of the molecular gas in the cloud (Leroy et al., 2025). A measure of the gravitational boundness of the clouds is the virial parameter α_{vir}, given by the ratio of the kinetic energy and the potential energy. It can be written in terms of the three-dimensional velocity dispersion $\sigma_{\mathrm{v,3D}}$, the radius of the cloud R and the mass of the cloud M (Federrath & Klessen, 2012)

$$\alpha_{\mathrm{vir}} = \frac{2K}{U} = \frac{5\sigma_{\mathrm{v,3D}}^2 R}{3GM}, \tag{2.4}$$

where a larger virial parameter corresponds to less bound clouds, and for $\alpha_{\mathrm{vir}} < 1$ the cloud will collapse under its own gravity. The three-dimensional velocity dispersion is calculated taking both the turbulent motion and the speed of sound into account

$$\sigma_{\mathrm{v,3D}} = \sqrt{\sigma_{\mathrm{turb}}^2 + c_{\mathrm{sound}}^2}. \tag{2.5}$$

Most theoretical models of star formation predict a higher star formation efficiency for lower virial parameters (Federrath & Klessen, 2012), since more bound clouds are denser and thus expected to collapse faster, leading to more stars being formed.

Once stars have formed, they will strongly influence the gas around them. Stars are formed with different masses following a distribution called the initial mass function (Chabrier, 2003). Massive stars will emit large amounts of energy through UV radiation, heating and ionising the gas around them, a process called stellar feedback. When the most massive stars explode in supernova (SN) explosions, they further disperse the gas around them, injecting energy into the turbulent movement of the gas. All of these effects change the surroundings and distribution of gas in the galaxy, making SF a dynamic process that responds to SFs in the past. The exact implementation of feedback for this work is detailed in Section 3.1

2.2 Star formation models and the problem of efficiency

In simulations, SF is modelled cell-by-cell following the Schmidt law for SF

$$\dot{\rho}_\star = \epsilon_{\rm ff} \frac{\rho_{\rm mol}}{\tau_{\rm ff}}, \tag{2.6}$$

which gives the change in density of stellar material based on the local SFE per free-fall time (Grisdale et al., 2019). The difference in SF models now depends on what $\epsilon_{\rm ff}$ is chosen for the cells. Determining this local $\epsilon_{\rm ff}$ is not a trivial task since, in galaxy-scale simulations, most of the physics governing star formation occurs below the simulation's resolution limit. Simplified treatments of complex physics must be implemented to model the SFE as accurately as possible. An ongoing problem in modelling SFE is that most models produce too high observed $\epsilon_{\rm ff}$ (e.g. Federrath & Klessen (2012)).

2.2.1 Fixed efficiency models

The simplest model sets a fixed efficiency for all cells. This is a major assumption that ignores the conditions of a star-forming cloud. These models are computationally simple, running faster without the need to compute additional hydrodynamic parameters. They can also serve as good benchmarks, allowing comparison of different input efficiencies without changing other parameters. This is also useful since some of the other parameters used for more complex models are approximations, introducing further errors. Historically, fixed efficiency models are the most commonly used in simulations.

2.2.2 The Padoan et al. (2012) "simple" model

Padoan et al. (2012) argue that in star-forming regions in GMCs, $\epsilon_{\rm ff}$ does not strongly depend on $\mathcal{M}_{\rm s}$. This follows their claim that there is not much variation of the Mach number in the typical star-forming interstellar medium (ISM). They propose a star formation model that only takes the free-fall time and dynamical time $\tau_{\rm dyn} \equiv R/2\sigma_{\rm v}$ into account, making computations faster and more straightforward. This argument is based on adaptive mesh refinement (AMR) simulations carried out by Padoan et al. (2012). The proposed model can be rewritten to depend on $\alpha_{\rm vir}$

$$\epsilon_{\rm ff} = \epsilon \exp\left(-1.6 \frac{t_{\rm ff}}{t_{\rm dyn}}\right) = \epsilon \exp\left(-1.6\sqrt{\alpha_{\rm vir}}\right). \tag{2.7}$$

where ϵ is the fraction of mass turned into a star during a collapse, accounting for winds and ejecta. Models treating star formation in this way will henceforth be referred to as PN models.

2.2.3 Federrath Klessen (2012) multi free fall KM model

More complex models seek to account for the properties of GMCs when modelling SF. This is done by assuming the gas inside the GMCs follows a lognormal probability density function given by

$$p(s) = \frac{1}{\sqrt{2\pi\sigma_{\rm s}^2}} \exp -\frac{(s-\bar{s})^2}{2\sigma_{\rm s}^2}, \tag{2.8}$$

where

$$s \equiv \ln\left(\frac{\rho}{\bar{\rho}}\right) \tag{2.9}$$

is the logarithmic density, σ_s the standard deviation of the logarithmic density, and a bar above a quantity denotes the average value (Kretschmer & Teyssier, 2020). Here, $\sigma_{\rm s}$ is calculated from other parameters as

$$\sigma_{\rm s} = \ln\left(1 + b^2\mathcal{M}^2\right), \tag{2.10}$$

with b being the turbulent forcing parameter, a parameter modelling the type of forcing to sustain and create the turbulence of the gas. It ranges from $b = 1/3$ for purely solenoidal forcing (divergence-free) to $b = 1$ for purely compressive forcing (curl-free) (Federrath & Klessen, 2012). The models outlined by Federrath & Klessen (2012) define a critical density $s_{\rm crit}$ and treat molecular regions that exceed this density threshold as collapsing and converting all of their mass into stellar mass. This gives the local star formation efficiency as

$$\epsilon_{\rm ff} = \frac{\epsilon}{\phi_{\rm t}} \int_{s_{\rm crit}}^{\infty} \frac{\tau_{\rm ff}(\bar{\rho})}{\tau_{\rm ff}(\rho)} \frac{\rho}{\bar{\rho}} p(s) ds, \tag{2.11}$$

where ϵ is the fraction of mass accreted onto protostellar cores similar to ϵ in the PN model, and $\phi_{\rm t}$ accounts for uncertainties in the free-fall time. This integral has the solution

$$\epsilon_{\rm ff} = \frac{\epsilon}{\phi_{\rm t}} \exp\left(\frac{3}{8}\sigma_{\rm s^2}\right)\left[1 + {\rm erf}\left(\frac{\sigma_{\rm s}^2 - s_{\rm crit}}{\sqrt{2\sigma_{\rm s}^2}}\right)\right]. \tag{2.12}$$

The model introduced by Krumholz & McKee (2005) and modified by Federrath & Klessen (2012) defines the critical density by comparing the sonic scale $\lambda_{\rm s}$ with the Jeans length $\lambda_{\rm J}(\bar{\rho})$ evaluated at the mean density

$$s_{\rm crit} = 2\ln\left(\phi_{\rm x}\frac{\lambda_{\rm J}(\bar{\rho})}{\lambda_{\rm s}}\right), \tag{2.13}$$

where $\phi_{\rm x}$ is a numerical parameter accounting for the uncertainty in the exact scale where collapse sets in. The sonic scale marks the transition between supersonic and subsonic turbulence and is defined as

$$\lambda_{\rm s} = 2R\left(\frac{c_{\rm s}}{\sigma_{\rm v,3D}}\right)^{\frac{1}{p}}, \tag{2.14}$$

with $c_{\rm s}$ the speed of sound, $\sigma_{\rm v,3D}$ the three dimensional velocity dispersion, and $p \approx 0.5$ as determined from observations. The Jeans length is the length at which thermal pressure can no longer support gravitational collapse, as given by

$$\lambda_{\rm J}(\rho) = \left(\frac{\pi c_{\rm s^2}}{G\rho}\right). \tag{2.15}$$

The expressions can be rewritten in terms of the sonic Mach number $\mathcal{M}_{\rm s}$ as done by Federrath & Klessen (2012) to obtain

$$s_{\rm crit,\ FK} = \ln\left[\alpha_{\rm vir}\frac{2\mathcal{M}^4}{1+\mathcal{M}^2}\right]. \tag{2.16}$$

The local efficiency $\epsilon_{\rm ff}$ for this model, henceforth referred to as FK model, is given by using this critical density in the general solution given by Equation 2.12. The numerical parameters $\phi_t = 1/0.49$ and $\phi_x = 0.19$ are chosen based on the best fit parameters to the simulations of driven turbulence by Federrath & Klessen (2012).

2.2.4 Kretschmer & Teyssier (2020) decalibrated FK model

Kretschmer & Teyssier (2020) discusses a 'decalibrated' version of the FK model by setting the parameter $1/\phi_{\rm t} = 1$ and updating the critical density to treat gas with a sonic Mach number $\mathcal{M}_{\rm s} < 1$. Removing the dependence on free parameters, which are calibrated on simulations, is what makes this decalibrated. This is done as the free parameters from simulations might not be how the real ISM behaves. For gas with Mach numbers below unity, the collapse criterion requires the entire cloud to collapse (i.e., $s_{\rm crit} = \ln(\alpha_{\rm vir})$). This gives us

$$s_{\rm crit,\ FKdec} = \ln\left[\alpha_{\rm vir}\left(1 + \frac{2\mathcal{M}^4}{1+\mathcal{M}^2}\right)\right], \tag{2.17}$$

which is used in Equation 2.12 with the numerical prefactor $1/\phi_{\rm t} = 1$. This model is referred to as decalibrated FK model in the remainder of the text. The resulting efficiency for this model, along with the ones discussed above as a function of $\alpha_{\rm vir}$ and $\mathcal{M}_{\rm s}$ are shown in Figure 2.1. It can be seen that the models produce very different surfaces. However, the models that don't have a fixed efficiency generally produce high input efficiencies. Input efficiencies match the order of observed SFEs per free-fall time on only a small domain of input parameters. The FK model in particular produces high input efficiencies for the majority of the domain. A possible regulation by feedback is discussed in Section 4.4. The decalibrated FK model shows a sharp transition of input efficiencies at $\alpha_{\rm vir} = 1$ for low Mach numbers. This is due to the modified collapse criterion for $\mathcal{M} < 1$, the FK model breaks down at those Mach numbers and should not be used in this regime. In general, the models that calculate the input efficiency show the theoretical trend that lower virial parameters and higher Mach numbers lead to higher SFEs.

2.2.5 Further models

There exists a range of other models that take different approaches to how the critical density is calculated or how the free-fall ratio $\frac{\tau_{\rm ff}(\bar{\rho})}{\tau_{\rm ff}(\rho)}$ is treated. A more detailed discussion on some of these models can be found in Federrath & Klessen (2012). An important consideration to take into account is that none of the models discussed here takes magnetic effects into account when calculating the critical density. Magnetic fields are thought to have a stabilising effect, reducing the magnitude of density fluctuations and thus decreasing the SFE. However, magnetic effects seem to only vary the SFE by a factor of two for realistic magnetic fields (Padoan et al., 2012; Federrath & Klessen, 2012).

2.3 Galaxy simulations

These SF models can be tested in various computational settings. Work has been done on testing them in isolated gas boxes, for example Federrath & Klessen (2012). One aspect that needs to be modelled, as it is below the resolution limit, is turbulent motion. This motion needs to be generated and sustained. Among others, work by Padoan et al. (2016) uses SN explosions to sustain the turbulence. However, no work so far considers global, galactic simulations where turbulence driving from large scale galactic dynamics is present. This work focuses on doing these simulations on isolated galaxies to fill this niche. There is a large body of work on different approaches to model galaxies that has been developing over the past decades. Many simulations take the dark matter simulations as given and try to model the behaviour and interaction of baryons on top of that (Naab & Ostriker, 2017). This is limited by computational resources and resolution limits, with many of the important physics occurring below the resolution limit. Simulations also differ in the way they resolve interactions. With smoothed particle hydrodynamics (SPH), the fluid is modelled with moving particles that contain information about the state of the fluid, which are calculated over a smoothed kernel of neighbouring particles. This allows

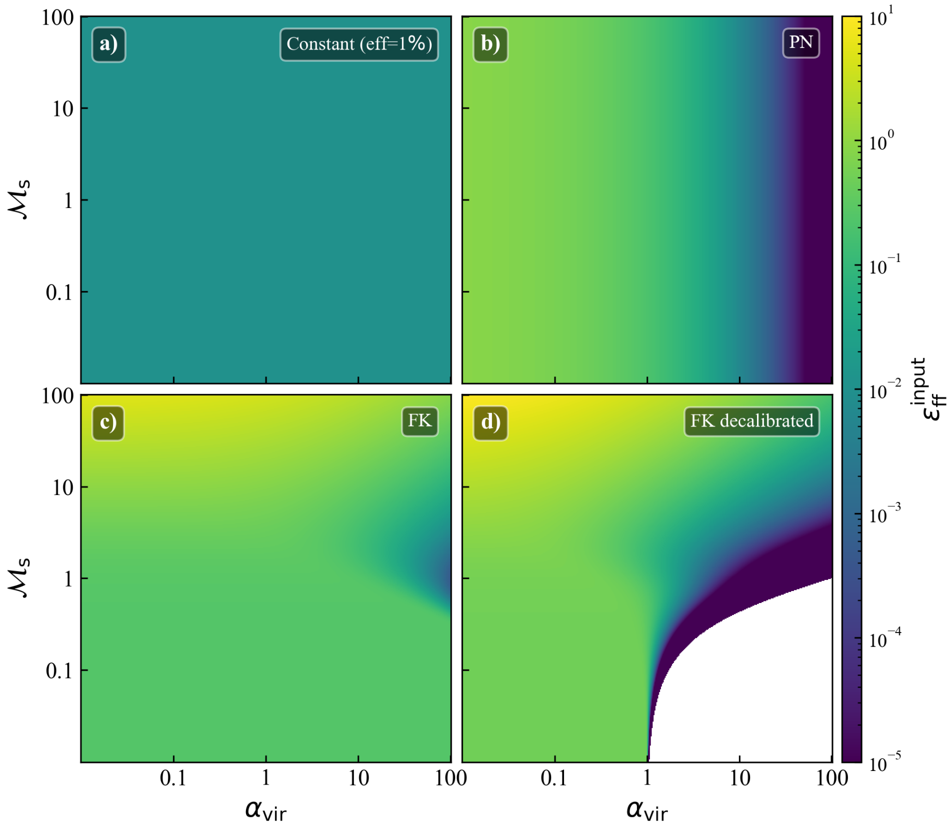

Figure 2.1: Shown are the input efficiencies $\epsilon_{\rm ff}^{\rm input}$ as a function of $\mathcal{M}_{\rm s}$ and $\alpha_{\rm vir}$ for different models. Panel a) shows an example of a fixed efficiency of 1%. In panel b), the simple model from Padoan et al. (2012) is shown. Panel c) shows the multi-free-fall KM model from Federrath & Klessen (2012) with the best fit parameters for ϕ_t and ϕ_x and a turbulent forcing parameter $b = 0.61$. The decalibrated FK model (Kretschmer & Teyssier, 2020) is shown in panel d) with $b = 0.65$. The forcing parameters are chosen as the mean values of the calculated values for each cell in the simulation. The white region in panel d) is due to the efficiency falling below a cutoff at 10^{-5}.

them to follow the flow of the fluid well; however struggles with resolving shock fronts due to the smoothing of particles (Teyssier, R., 2002). Mesh-based simulations have a fixed mesh on which the fluid equations are calculated, which allows them to model shock fronts better. To avoid having the same resolution in shock fronts as in low-density gas, AMR can be used. There, the mesh resolution is adapted based on some criteria to increase the resolution in areas of interest. A newer code, AREPO (Springel, 2010), introduces a moving mesh to combine the benefits of both approaches. A more comprehensive review on galaxy simulations and different codes can be found in Naab & Ostriker (2017). This thesis deals with the code RAMSES (Teyssier, R., 2002) outlined in Section 3.1.

2.4 Cloud-scale star formation in observations

In observations, star formation can only be observed at large scales for extragalactic observations. This makes it hard to track the properties of clouds and formed stars. As such, most measurements are taken over regions determined by the resolution power and quantities are then averaged across those regions.

The main insight into gas properties comes from the transition line emission of atoms and molecules. Radio telescopes like ALMA are sensitive to the wavelength at which CO transitions occur. For this reason, observations convert from CO to H_2 with models for conversion factors. The calculated quantities depending on molecular hydrogen densities are sensitive to this conversion factor (Leroy et al., 2025). Many simulations also model CO to match observations, but this is a complex field with many studies done to improve the models (e.g. Glover & Clark (2012)).

The cloud properties are determined from the CO-line. Mass and density can be calculated from the integrated CO-line luminosity, and the line width is used to determine the velocity dispersion (Sun et al., 2022). From this, all cloud-scale properties can be calculated in the same way as for the computational models. Since SF cannot be calculated outside of our galaxy by counting stars, observers need to estimate the formed stellar mass using tracers. Leroy et al. (2025) investigate PHANGS-ALMA data of galaxies, some of which are shown in Figure 2.2, by tracing H-α emissions and WISE 22 μm mid infrared emissions of surrounding dust. The H-α emissions are from ionised gas surrounding young massive stars (Hu et al., 2024) created by the strong UV emissions up until 5 Myr after SF. The mid infrared emissions are due to thermally heated dust surrounding stars that absorbed stellar radiation, tracing SF on a longer timescale (Belfiore et al., 2023).

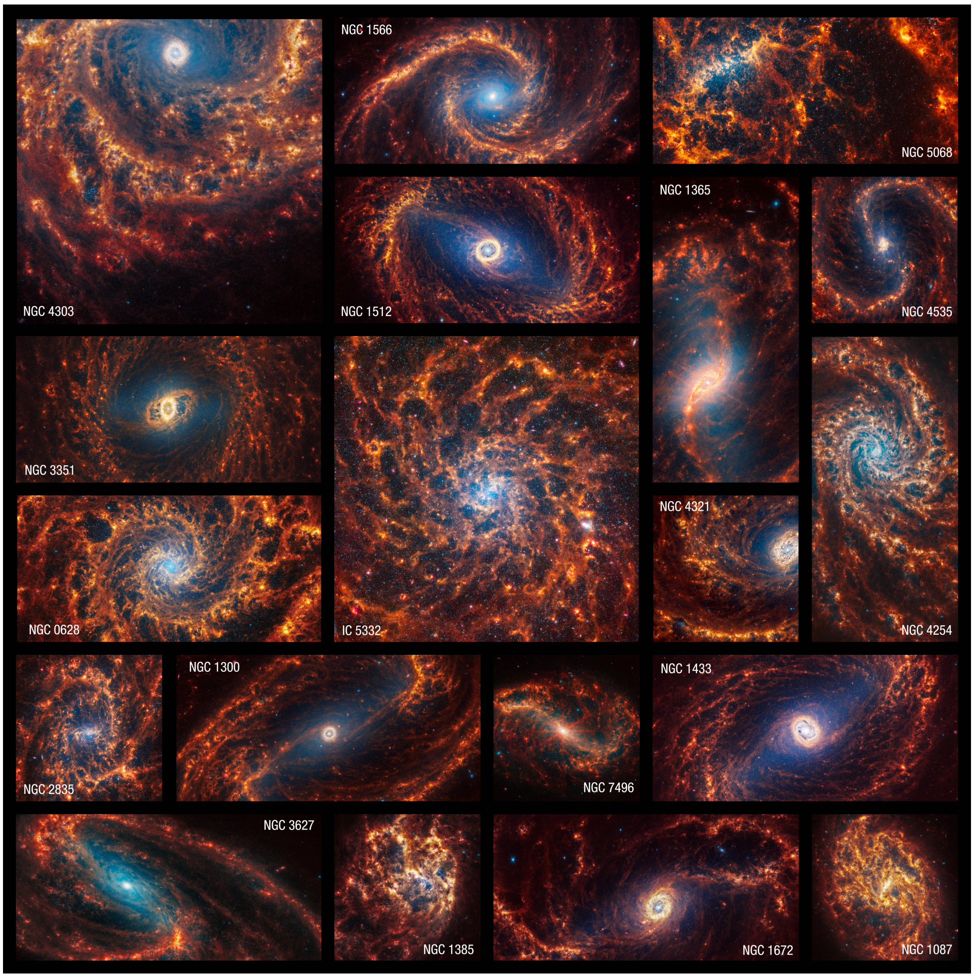

Figure 2.2: Near and mid-infrared depictions of some of the galaxies observed by the James Webb Space Telescope as a contribution to the PHANGS programme (NASA/ESA/CSA/STScI, 2023). Leroy et al. (2025) use, amongst others, those galaxies (except for NGC 5332 and NGC 1672) for their analysis.

Chapter 3

Method

3.1 Simulations

The simulations are computed with the N-body hydrodynamical code RAMSES. It models stars and dark matter as collisionless particles, whereas gas is modelled as a fluid following hydrodynamical equations. The code is based on AMR with a tree-based data structure (Teyssier, R., 2002). The N-body solver is based on collision-less N-body physics described by the Vaslov-Poisson equations for particles, and the hydrodynamics are solved with the second-order Godunov method (Teyssier, R., 2002). This leads to a data structure called a 'Fully Threaded Tree' (Khokhlov, 1998), where 'octs', the basic element of the simulation consisting of a group of cells, are stored for each refinement level. A more detailed description of how RAMSES models galaxies can be found in Teyssier, R. (2002).

The simulations are set up similarly to Ejdetjärn et al. (2022). The initial conditions are based on the AGORA isolated disc galaxy (Kim et al., 2014, 2016) set up as a Milky Way mass galaxy with a gas fraction of 10%. The total disc mass is $M_{\text{disc}} = 4.5 \cdot 10^{10}$ $\text{M}_\odot$. The halo has a viral mass $M_{200} = 1.1 \cdot 10^{12}$ $\text{M}_\odot$ within $R_{200} = 205$ kpc. The density of gas and stars initially follows exponential profiles with scale length $r_\text{d} = 3.4$ kpc and scale height $h = 0.1\ r_\text{d}$. The bulge-to-disc mass ratio is 0.125.

The mesh refines when the baryonic mass of a cell exceeds eight times the initial gas mass resolution or if it contains more than eight dark matter particles. The finest resolution limit achieved is approximately 8 pc. Star formation is handled according to the Schmidt law, Equation 2.6. All stars are created as star particles with a mass of 500 $\text{M}_\odot$, treated as a single age stellar population following the initial mass function (IMF) by Chabrier (2003). Feedback accounts for the injection of energy, momentum and mass from the stars back into the ISM. The feedback processes are implemented following Agertz et al. (2013) and treat stellar winds, SNe, mass loss through low mass stars and, in the runs that have radiative transfer (RT) enabled, radiation pressure. The RT runs are done to investigate the effects on the SFE, following similar RT methods as Agertz et al. (2020).

For all simulations, both a fiducial run, with feedback strengths according to the literature, as well as a boosted run, with twice the feedback strength, are performed. This means all energy and momenta that are injected through feedback are boosted by this factor. The 1% fixed efficiency model and the 100% fixed efficiency model also have a boosted run with an additional increase of SN feedback by a factor of 10. The time for which the simulations are run differs between 150 and 300 Myr. This does not affect the results besides the number of datapoints for each run and is a result of the computing times and resources available for the simulations.

All simulations output a snapshot of the state of the galaxy every 5 Myrs. These snapshots will be analysed as outlined in the following sections.

Since galaxies are isolated, we exclude the effects of mergers or interactions with satellite galaxies. There is also no treatment of the cosmological evolution of the galaxies. The simulations only track the total gas density and do not take into account chemical compositions. Total metallicity and the metals N, O and Fe are tracked.

3.2 Mock observations

The mock observations are carried out following the method of observation described by Leroy et al. (2025). After the analysis, the different outputs of the simulations are combined. This is done to increase the number of data points per model, similar to observing the same galaxy at different stages of evolution. The resolution limit of the simulations is smaller than that of the observations, around 8 pc vs. around 150 pc, so to have a sensible comparison with the observational data, the lower resolution of the observations is adopted. This means that information is being lost in favour of a direct comparison.

3.2.1 Cloud-scale properties

The gas is first filtered on a cell-by-cell basis according to simple temperature and density cuts to filter for molecular hydrogen. Only gas denser than $n_{\rm th} = 50$ cm^{-3} and a colder than $T_{\rm th} = 100$ K is included. These cuts are varied to investigate the sensitivity to the molecular hydrogen selection, and results are discussed in Section 4.8. The filtered gas is then projected along the line of sight, in the case of simulations, the line perpendicular to the plane of the galaxy. To match the observational resolution of Leroy et al. (2025) the galaxy is divided into 150 pc squares on which $\tau_{\rm ff}$, $\sigma_{\rm v}$ and $\alpha_{\rm vir}$ are calculated, from $\Sigma_{\rm mol}$ using Equation 2.3, Equation 2.5 and Equation 2.4 respectively.

Since clouds are not tracked individually in this work, the cloud-scale parameters $\Sigma_{\rm mol}$, $\tau_{\rm ff}$, $\sigma_{\rm v,3D}$ and $\alpha_{\rm vir}$ are mass averaged over 1.5 kpc regions. These mass averages correspond to the mean value a cloud in that region has. The 1.5 kpc regions are chosen to be square, contrary to the hexagons used by Leroy et al. (2025), to simplify the analysis and avoid edge overlaps. This methodological difference is not expected to significantly change the results of the analysis. Then, a completeness cut is employed to filter out regions with a mass averaged surface density $\langle\Sigma_{\rm mol}\rangle < 20$ $\rm M_\odot$ corresponding to a resolution limit by Leroy et al. (2025). The downscaling and averaging process is shown in Figure 3.1. The calculated quantities for the two resolutions are summarised in Table 3.1.

3.2.2 Star formation properties

The simulations give detailed information about every SF event; however, to match the data of the observations, the SFR surface density is calculated on the same 1.5 kpc squares as the cloud-scale gas properties with

$$\Sigma_{\rm SFR} = \frac{M_\star}{t_\star L^2}, \tag{3.1}$$

where $L = 1.5$ kpc and $M_\star$ is the mass of stars younger than a time cut $t_\star$. Since Leroy et al. (2025) are using Hα and 22μm WISE4 maps, which trace young stars, $t_\star = 7$ Myr is chosen. The effects of different time cuts are investigated in Section 4.8. From the SFR, $\tau_{\rm dep}$ and $\epsilon_{\rm ff}$ can then be calculated for the 1.5 kpc regions.

All calculated SF quantities with their units are summarised in Table 3.1.

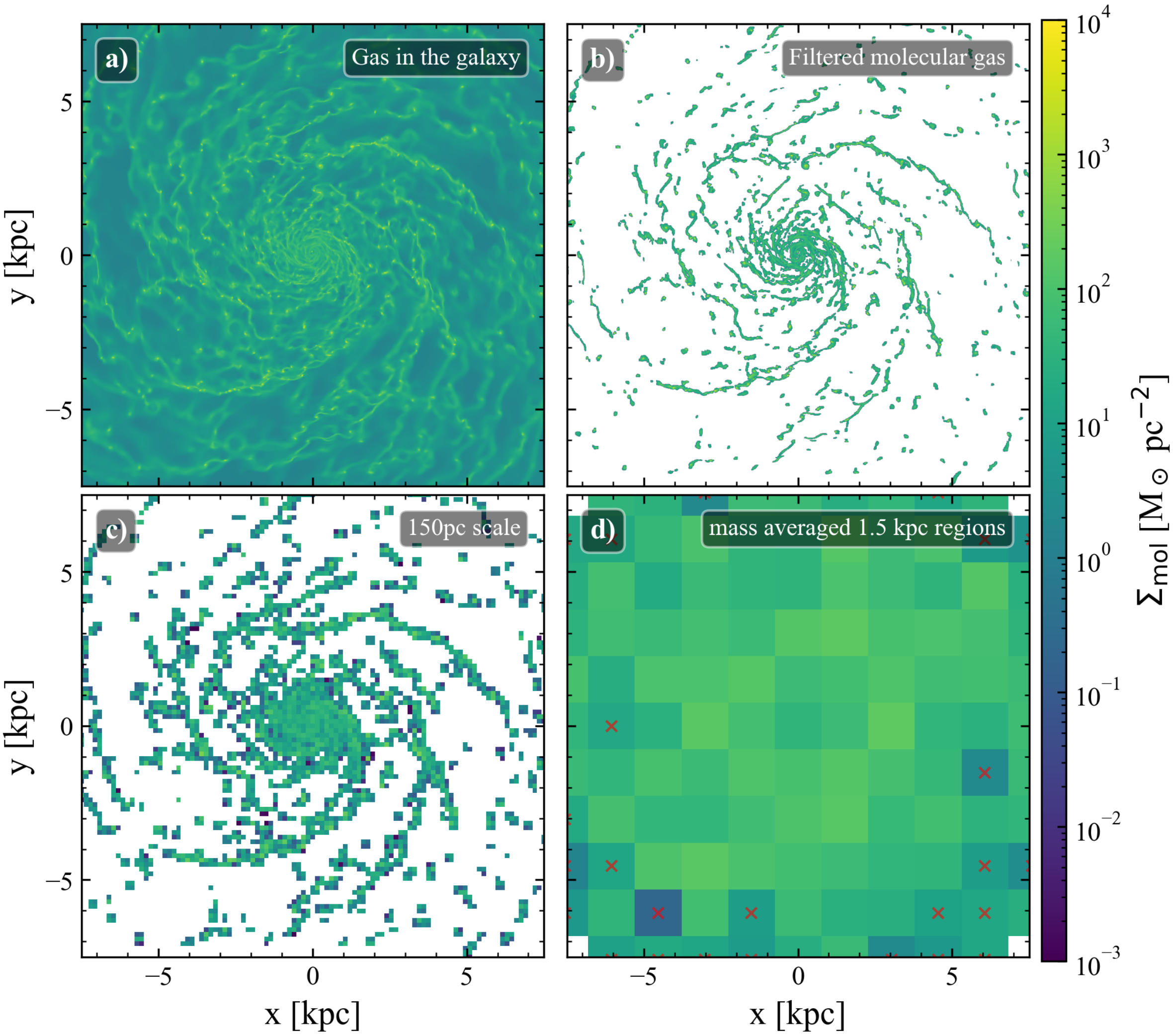

Figure 3.1: Depiction of the selection process and rebinning to the desired resolutions. The example shows one output of the fiducial eff001 model. Panel a) shows the surface density of all the gas in the galaxy. In panel b), the molecular gas selection cut has been applied before the projection with $n_{\mathrm{th}} = 50\ \mathrm{cm}^{-3}$ and $T_{\mathrm{th}} = 100$ K. Panel c) depicts the molecular surface density at the 150 pc scale, the smallest resolution Leroy et al. (2025) use in their main analysis. Finally, panel d) shows the mass-averaged molecular surface density for the 1.5 kpc regions. Marked with the red crosses are the regions that do not pass the completeness cut of $\langle\Sigma_{\mathrm{mol}}\rangle > 20\ \mathrm{M}_\odot\ \mathrm{pc}^{-2}$.

Table 3.1: Summary of calculated quantities.

	Quantities on 150pc scale	
$\Sigma_{\rm mol}$	Surface density of the molecular gas	$M_\odot$ pc^{-2}
$\tau_{\rm ff}$	Free fall time of the molecular gas, Equation 2.3	yr
$\sigma_{\rm v,3D}$	Velocity dispersion, Equation 2.10	km s^{-1}
$\alpha_{\rm vir}$	Virial parameter, Equation 2.4	dimensionless
	330x330 grid for every output of each simulation	
	Averaged quantities on 1.5 kpc scale	
$\langle\Sigma_{\rm mol}\rangle$	Mass averaged molecular surface density	$M_\odot$ pc^{-2}
$\langle\tau_{\rm ff}\rangle$	Mass averaged free fall time	yr
$\langle\sigma_{\rm v,3D}\rangle$	Mass averaged velocity dispersion	km s^{-1}
$\langle\alpha_{\rm vir}\rangle$	Mass averaged virial parameter	dimensionless
$\Sigma_{\rm SFR}$	Surface density of star formation rate, Equation 3.1	$M_\odot$ yr^{-1} pc^{-2}
$\tau_{\rm dep}$	Molecular depletion time, Equation 2.1	yr
$\epsilon_{\rm ff}$	Star formation efficiency per free fall time, Equation 2.2	dimensionless
	33x33 grid for every output of each simulation	

Chapter 4

Results and discussion

4.1 Visual comparison of models

Figure 4.1 shows the gas surface density in the central galactic region of four different simulations run with different SF models at similar output times.

All parameters except for the SF model and the feedback strength are kept constant. Comparing the low-efficiency fiducial model (upper-left panel) with the high-efficiency model with additionally boosted feedback (lower-left), one can see that the low-efficiency model produces clumpy gas with several small high-density regions. In contrast, the other model produces disrupted and diffuse gas. The two other models (shown in the right panels) produce results somewhere in between. The clumpy gas is caused by the fact that, due to the low efficiency of SF, SF is not

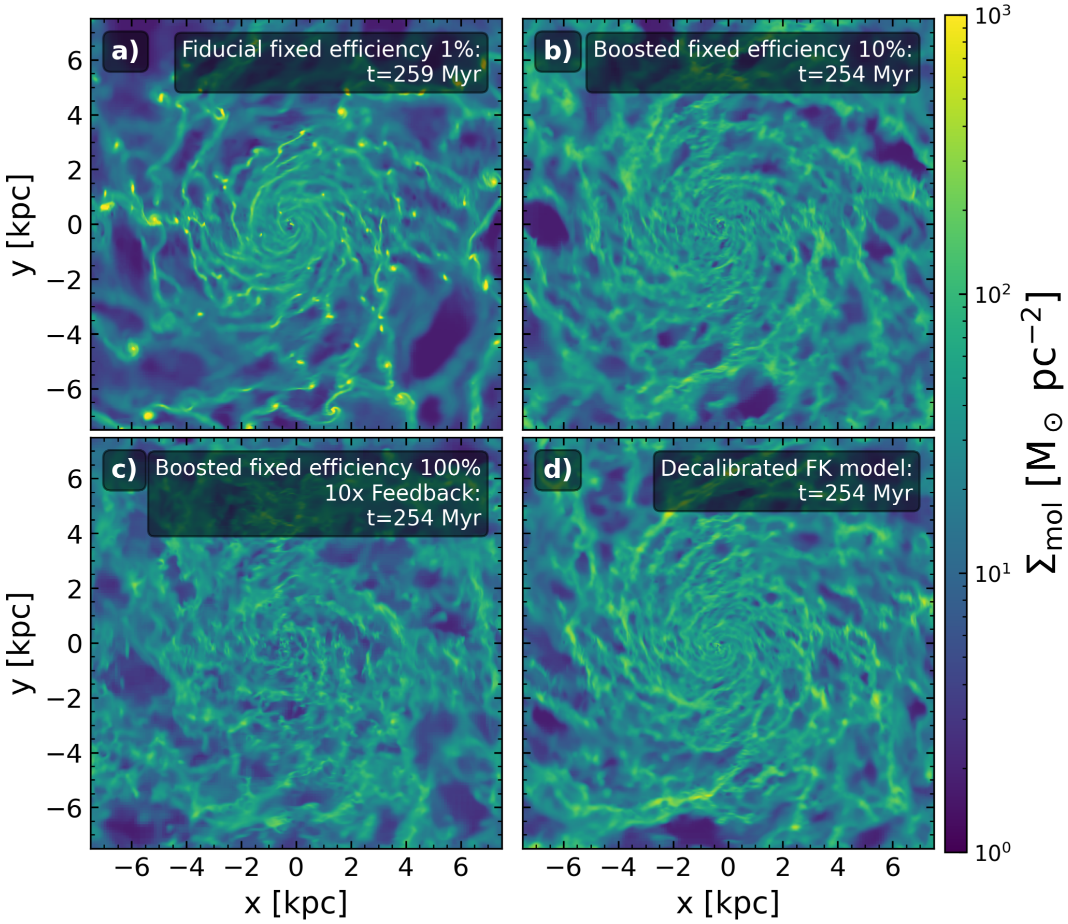

Figure 4.1: Surface density of different models at similar output times. Panel a) shows the fiducial run for the eff001 model. This is the lowest-efficiency model run in this work. Panel b) shows the galaxy run with a boosted eff01 model, and panel c) depicts the boosted eff1 model with an additional increase of the SN feedback strength by a factor of 10. The final panel shows the decalibrated FK model with a similar input efficiency to the first model.

correlated enough in time to allow for feedback from young massive stars to disrupt the clouds. More intense SF is needed to break them up, or stronger feedback. It is shown in the next section that this leads to an increase in global SFR. In comparison, the boosted high efficiency model has many more stars formed in each cloud, causing more feedback events, which then have an increased strength, dispersing most of the clouds and leaving behind low-density turbulent gas.

These are global responses of the gas leading to large-scale effects that change the distribution of gas in the galaxy, influencing future SF. It is expected that different SF models lead to global changes, but these results confirm that it is not enough to investigate at local effects to determine if a model can match observations.

4.2 Global star formation rate

The global SFR for every simulation run is shown in Figure 4.2. The stellar ages are taken

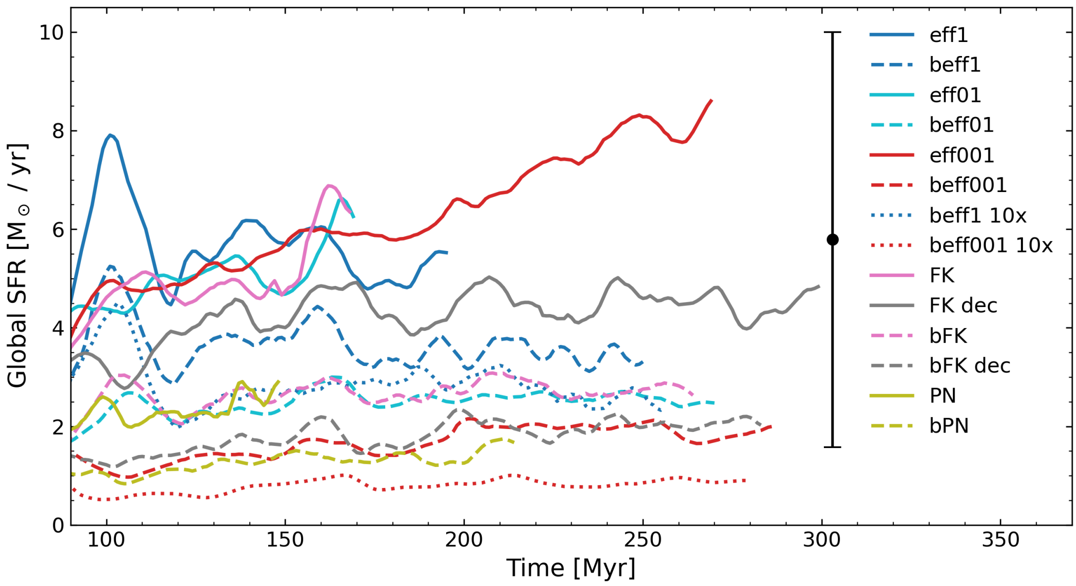

Figure 4.2: The global SFR for all run simulations 90 Myr after the start of the simulation onwards. The SFR is calculated on 7 Myr bins centred on every Myr. Solid lines show the fiducial models, boosted models are indicated by a dashed line, and the dotted lines represent boosted models with an increased SN feedback strength of a factor 10. The Milky Way has a global SFR of around 2 $M_{\odot}yr^{-1}$ (Soler et al., 2023). The black errorbar shows the spread in SFR in Milky Way-mass galaxies (Whitaker et al., 2012).

from the final output of each simulation, and the SFR is calculated at 1 Myr intervals from the formation of the first star, using 7 Myr bins centred on each evaluation time. It can be seen that the feedback strength plays a crucial role in setting the global SFR. All models with boosted feedback (indicated by the dashed and dotted lines) show lower SFRs than their fiducial counterparts. This is an expected result, as higher feedback means more dispersion of gas, leading to fewer star-forming regions. Less trivial is the result that this effect is stronger the lower the input efficiency of the model. One might expect that in high-efficiency models, due to the increased efficiency, more stars form, and as such, feedback matters more. However, it seems likely that the gas in the high-efficiency models is already dispersed, so that the increased feedback strengths have little effect. In contrast, as seen above, the eff001 model has very dense regions that can be affected by feedback effects, thus showing a strong response to changes in feedback strength.

There is also an oscillatory behaviour of the SFRs, resulting from the fact that periods of increased SF are followed by increased feedback effects that disperse the gas and lower the SFR.

Another non-trivial result is that the fiducial eff001 model shows the largest global SFR despite its low intrinsic efficiency. This is because a low local SFE, which naively can be anticipated to reduce SF globally, leads to more long-lived star-forming clouds due to a weaker effect of feedback. The sum of their SFRs is the global SFR, which is higher than other models by a factor of a few.

The Milky Way has a global SFR of around 2 $M_\odot$ yr^{-1} (Soler et al., 2023), with variations of around half a solar mass per year depending on the measurement (Murray & Rahman, 2010; Licquia & Newman, 2015; Soler et al., 2023). Investigating galaxies with similar stellar masses to the Milky Way, the SFRs range from 1.58-10 $M_\odot$ yr^{-1}, meaning all models produce reasonable global SFRs (Whitaker et al., 2012). This makes it difficult to evaluate the models based on the global SFR and requires us to investigate a combination of global and cloud scales. All fiducial models, except for the decalibrated FK model and PN model, also have similar SFR to each other. Hopkins et al. (2011) found a similar independence of the SFR of the fixed efficiency models in Milky Way simulations. Other works in the literature also show results consistent with our findings, indicating that if simulations include feedback, the gas and SF will self-regulate to achieve values of SFR of a few solar masses per year fairly independent of the SF model (Hopkins et al., 2013).

4.3 Distribution of cloud scale properties

Figure 4.3 shows the distribution of cloud scale properties for different models. The fiducial simulations are shown with solid lines, boosted simulations with a dashed line, and dotted lines indicate an increase of feedback strength by a factor of 10. The black line indicates the observed data by Leroy et al. (2025). Both the lower limit of the surface density $\langle \Sigma_{\rm mol} \rangle$ and the upper limit of the free fall time $\langle \tau_{\rm ff} \rangle$ are set by the completeness cut $\langle \Sigma_{\rm mol} \rangle > 20$ $\mathrm{M}_\odot$, introduced by Leroy et al. (2025) and adopted in this work.

It can be seen that the high-efficiency model (left column) produces cloud-scale properties that do not match the observed data. The gas tends to have too low surface densities due to too effective cloud disruption pushing the gas apart, leading to a narrow distribution of $\langle \tau_{\rm ff} \rangle$. It is also too turbulent, showing both too large $\langle \alpha_{\rm vir} \rangle$ and $\langle \sigma_{\rm 3D} \rangle$. The mismatch with the observed data is even greater for increased feedback strengths. The left column shows more noise since most of the gas does not survive the completeness cut, and there are fewer cloud regions plotted.

Generally, for all models, increasing the feedback produces too turbulent and unbound gas. However, for both the eff001 model and the PN model, the boosted runs show a better match to the surface densities and free-fall times compared to the fiducial ones. The PN model, decalibrated FK model, and eff001 model show a reasonably good match for all cloud-scale parameters. Surprisingly, the PN model and especially the eff001 model are able to reproduce these values so well despite their simplistic assumptions in their SF model.

The PHANGS-ALMA data have a spectral resolution limit of around 2.5 km/s for their velocity dispersion (Rosolowsky et al., 2021). This, however, does not affect our analysis as the simulated data lies above this threshold, except for the eff1 model.

It can also be seen here that the effects of feedback on these local scales are much smaller than what is seen on the global scale. This again is indicative of the fact that feedback changes the distribution of the gas, leading to fewer star-forming regions, but it does not greatly affect the conditions within those regions.

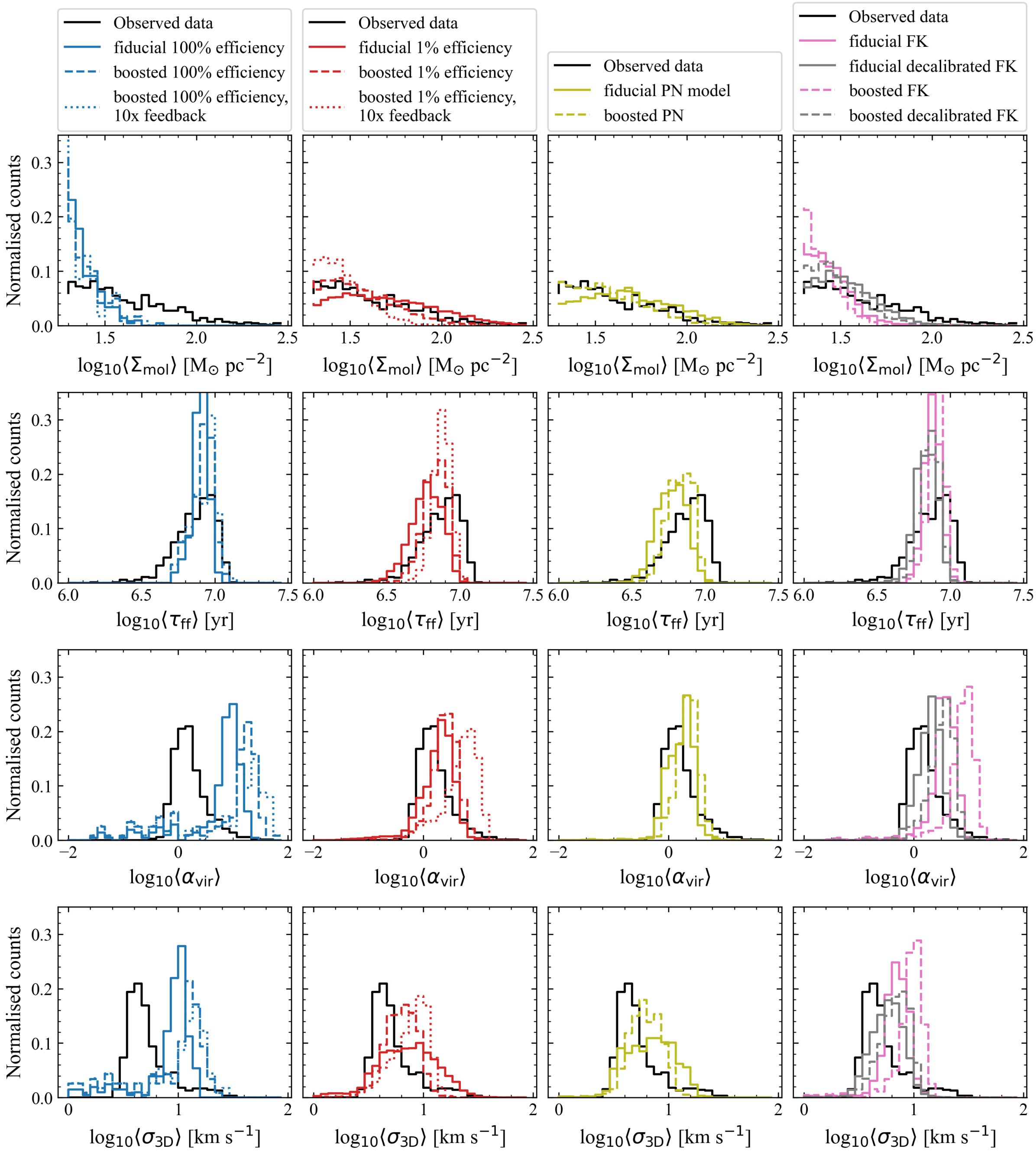

Figure 4.3: Distribution of cloud scale parameters on the 1.5 kpc scale shown for the different models. In all panels, the solid lines indicate the fiducial model, the dashed lines the boosted model and the dotted lines the models where the SN feedback was increased by a factor of 10. The leftmost column shows models with fixed input efficiency $\epsilon_{\rm ff}^{\rm input} = 100\%$ and the second column has fixed $\epsilon_{\rm ff}^{\rm input} = 1\%$. In the third column, the PN models (Federrath & Klessen, 2012) are shown, and the final column shows both the initial FK model (pink) (Federrath & Klessen, 2012) and the decalibrated FK model (gray) (Kretschmer & Teyssier, 2020). The black dashed line indicates the observed data from Leroy et al. (2025).

4.4 Distribution of star formation parameters

The models that take cloud-scale properties into account for SF depend on α_{vir} and $\mathcal{M}_{\mathrm{s}}$. These parameters were tracked for the FK model and decalibrated FK model, and their distribution is shown in Figure 4.4. The figure shows both on what domain SF takes place and which input efficiencies are calculated for the different models. The input efficiencies represent the analytical efficiencies at the time of SF and are not to be confused with the observed efficiencies, which have a time delay and are subject to observational biases. Contours containing 50%, 80% and 95% of

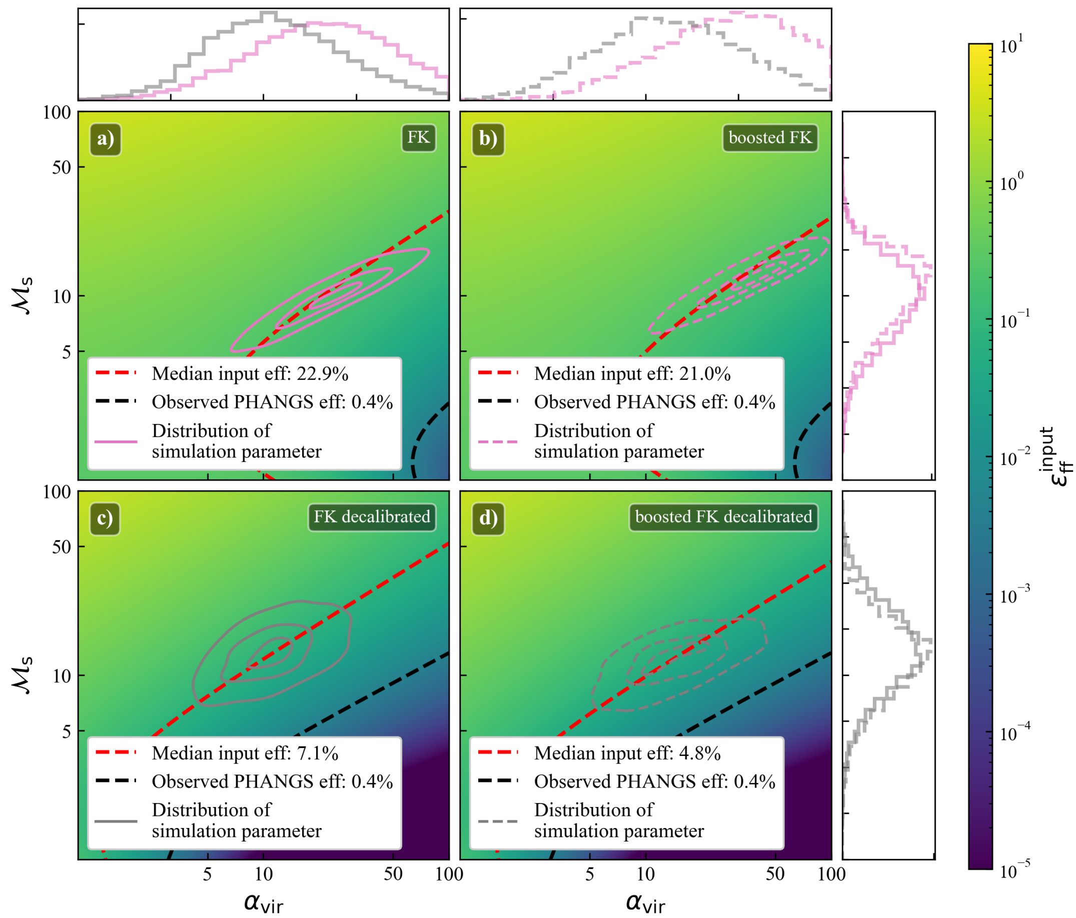

Figure 4.4: Input SFE per free fall time as a function of sonic Mach number and virial parameter. The upper panels show the surface for the FK model (Federrath & Klessen, 2012) and the lower panels show the decalibrated FK model (Kretschmer & Teyssier, 2020). Overlaid in gray and pink are the contours of the distribution for both the fiducial (left panels) and boosted (right panel) simulations. The contours enclose 50%, 80% and 95% of the data, respectively. The red line depicts the values along the surface that correspond to the median efficiency. The black line depicts the observed efficiency by Leroy et al. (2025).

the data are overlaid on the theoretical model, calculating the input efficiency. Both the fiducial (left panels) and the boosted (right panels) runs use the same theoretical model. The red dashed line indicates the median input efficiency of that model, whereas the black dashed line shows the observed efficiency by Leroy et al. (2025). It needs to be noted that the observed efficiency is a slightly different quantity, and a comparison to the input efficiency is not straightforward. It is included here to serve as a guideline of the magnitudes.

Two effects influence the input efficiencies, as can be seen in Figure 4.4. The main effect comes from the fact that the different theoretical models give different input efficiencies for similar distributions of α_{vir} and $\mathcal{M}_{\mathrm{s}}$, causing the main difference between the top and bottom panels. A more subtle effect arises since different models and feedback strengths change the properties of the gas in the galaxy, causing different distributions of the star formation parameters. However, these effects are small and do not greatly influence the input efficiencies. Especially, the FK model is flat in the region around the distribution, and increasing feedback has only a minor effect on the efficiency. The effect of feedback is larger in the decalibrated FK model.

The distribution of the parameters also confirms that GMCs have virial parameters and sonic mach numbers of around ten, similar to what previous work found (Kretschmer & Teyssier, 2020). Since almost all regions have $\mathcal{M}_s > 1$, the modification of the decalibrated FK model to treat gas below that has only a minor impact on SF.

4.5 Comparison of efficiency and virial parameter with the results from Leroy et al. 2025

The following section shows the observed efficiency $\epsilon_{\rm ff}^{\rm obs}$ depending on the virial parameter $\alpha_{\rm vir}$ for some selected models. The remaining models are shown in Appendix A. This is a direct comparison with one of the main results obtained by Leroy et al. (2025). Figure 4.5 shows the fiducial runs for the fixed efficiency models. Here, it can be seen that higher input efficiencies

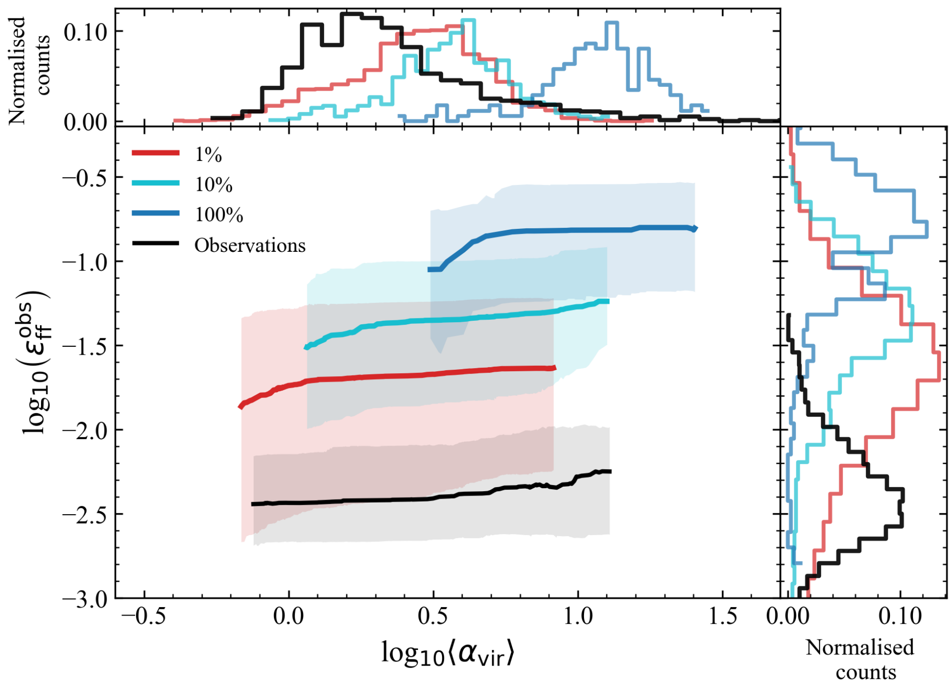

Figure 4.5: Observed efficiency plotted against the virial parameter for the fiducial fixed efficiency models. The solid lines indicate the running median of each model, while the shaded region marks the 16% to 84% quartile regions. Shown in black is the observational data from Leroy et al. (2025). The histograms in the margins show the normalised distributions of the quantity plotted along the respective axis for all models. Data in the central panel are shown only for bins containing at least 0.5% of the total data points.

lead to higher observed efficiencies and more unbound gas (higher $\alpha_{\rm vir}$). None of the fiducial fixed efficiency models matches the low efficiencies observed in the PHANGS-ALMA data. The eff001 model has some regions that are within one standard deviation of the observed median, but the overlap is small. All models show larger efficiencies and a larger spread than the observed data. This is surprising, since the input efficiencies are fixed to one value and the spread in the cloud scale parameters is not significantly different to the observed data. This means there is most likely another factor that is introducing the spread, which is not analysed here.

The fiducial runs for the more complex models are shown in Figure 4.6. Here, the PN model reaches a reasonable agreement with the observed data, although it is missing the high $\alpha_{\rm vir}$ tail that the observed data show. Another notable result is the fact that the PN model shows no noticeable correlation between the SFE and the virial parameter, even though the input efficiency model solely depends on $\alpha_{\rm vir}$. This means that while the missing high-$\alpha_{\rm vir}$ tail will affect the input efficiency, it might not affect the observed efficiencies.

All simulated models, in both the fiducial and boosted runs, reproduce the weak to non-existent correlation between $\epsilon_{\rm ff}$ and $\alpha_{\rm vir}$ seen in the observed data as well. That is, the simulations reproduce the observed data rather than the theoretical expectations. One possible reason for this is that there is a time delay between the formation of stars and the observation of tracers. This means that regions which show high tracers of SF have formed stars a few Myr ago and have since had time to disperse due to feedback. Therefore, the observed properties of star-forming regions do not compare directly to the properties the region had when it formed stars.

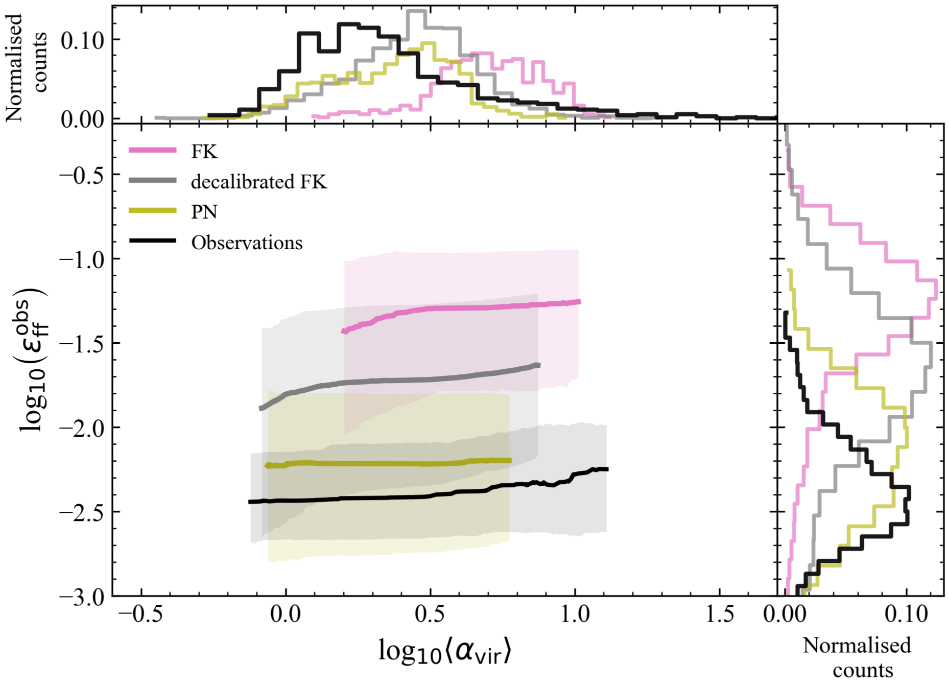

Figure 4.6: Similar plot to Figure 4.5. Shown are the FK model, decalibrated FK model and PN model.

4.6 Observed versus input efficiency

The input efficiencies do not directly correspond to the observed efficiencies, as shown in Figure 4.7. All simulated models are shown for both the fiducial and boosted runs. As discussed above, increasing feedback changes the input efficiencies for models that do not set a fixed efficiency. The strength of this change varies. A lower input efficiency does not directly correspond to a lower observed efficiency, which is notable in the FK model and eff001 model. However, there is a general trend that lower input efficiency correlates with lower observed efficiency. Also notable is that the effects of boosted feedback vary from model to model on both the observed efficiency and the input efficiency. These are surprising results that indicate that SFE is very dependent on the chosen model and that changing the feedback is not a simple process that can freely shift efficiencies. This is contrary to what some have previously argued, favouring high local efficiencies that are self-regulated by feedback (Semenov et al., 2016; Hopkins et al., 2011; Agertz & Kravtsov, 2015).

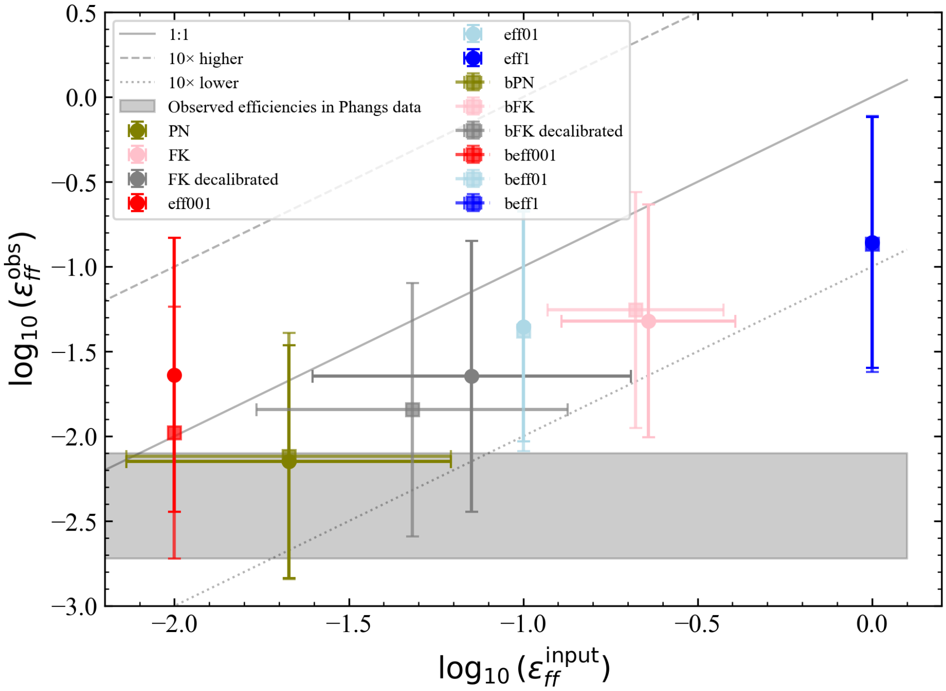

Figure 4.7: Observed efficiencies versus the input efficiencies for the different models. Shown are both the fiducial runs (spheres) and boosted (squares). The grey diagonal lines show the lines for direct, 10:1, and 1:10 correlation of the efficiencies. The shaded region indicates the median observed efficiency from Leroy et al. (2025) and one standard deviation away from the median.

Table 4.1: Factor by which feedback affects the listed quantity compared to the fiducial run. Factors in brackets denote the effect of increasing the SN feedback by a factor of ten compared to the fiducial.

Model	$\epsilon_{\rm ff}$	$\langle\Sigma_{\rm cloud}\rangle$	$\langle\tau_{\rm ff}\rangle$	$\langle\alpha_{\rm vir}\rangle$	$\langle\sigma_{\rm v,3D}\rangle$	$\tau_{\rm dep}$	$\Sigma_{\rm SFR}$
eff1	0.52 (0.43)	0.99 (0.98)	1.05 (1.10)	1.81 (1.71)	1.20 (1.18)	1.82 (2.40)	0.31 (0.13)
eff01	0.87	0.85	1.11	2.48	1.45	1.26	0.61
eff001	0.51 (0.46)	0.71 (0.59)	1.16 (1.27)	1.28 (2.71)	0.88 (1.12)	2.35 (2.82)	0.46 (0.40)
PN	0.93	0.75	1.16	1.29	0.88	1.29	0.59
FK	0.94	0.89	1.09	2.22	1.40	1.18	0.60
Decalibrated FK	0.68	0.88	1.07	1.68	1.20	1.52	0.73

4.7 Limits of stellar feedback

4.7.1 Stellar winds and supernova feedback

Stellar feedback can reduce the observed efficiency, as discussed in the previous sections. As seen in Figure 4.3, increasing the feedback changes the cloud-scale parameters, shifting them away from the observed values. The change in values due to feedback is small, changing parameters by a factor of around two. However, differences to observed efficiency values can range up to a factor of 35, in the case of the fiducial 100% fixed efficiency model. Table 4.1 shows the factor f by which the feedback changes various quantities Q for the different models;

$$f = \frac{Q_{\rm feedback}}{Q_{\rm fiducial}}.$$

For the eff001 model and eff1 model, the effect of the 10 times increased SN feedback is included in brackets. These factors vary from model to model but are, with some exceptions,

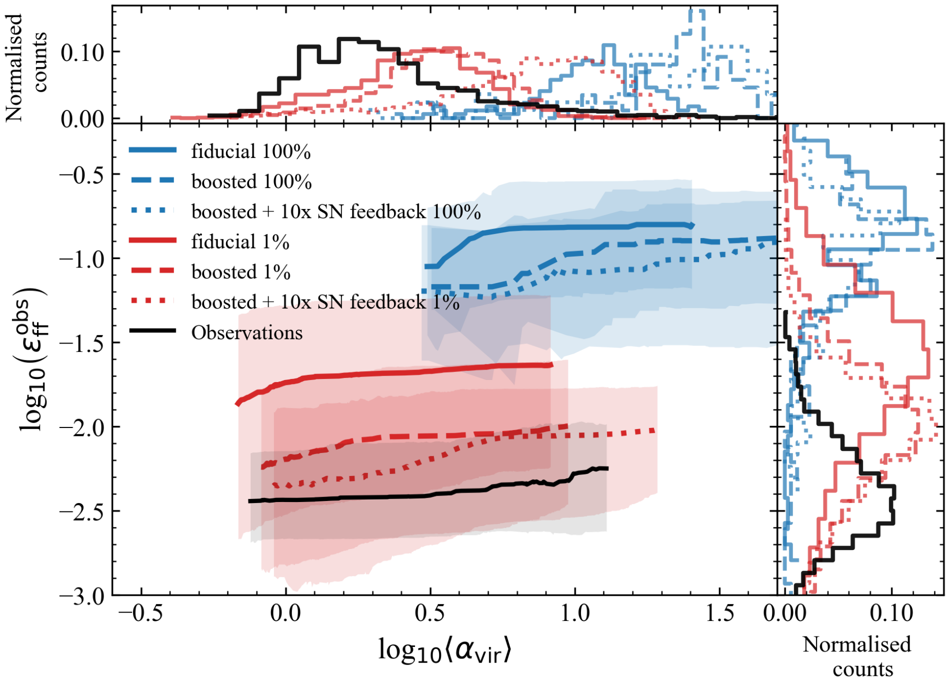

Figure 4.8: Similar plot to Figure 4.5 and Figure 4.6. Shown are the fixed efficiency models for 100% (blue) and 1% (red). The solid lines depict the fiducial models, dashed lines indicate boosted runs, and boosted simulations with additional increase of SN feedback are shown with dotted lines.

further away from unity for lower efficiency models. This might be due to the fact that high efficiency models produce enough SF events already to disperse the gas, so that increasing the feedback has little effect on the dispersed gas. Another effect is that a majority of the gas in the high efficiency models is excluded from the analysis due to the completeness cut, i.e. $\Sigma_{\rm mol} > 20$ $M_\odot/{\rm pc}^2$, meaning that regions where feedback is strong and SF active will not be included in the analysis.

Figure 4.8 shows the effect of increasing the feedback on the plots shown in the previous section for the eff001 model and eff1 model. It can be seen that it is possible to lower the efficiency of the lower-efficiency model to the observed SFE. Surprisingly, this is not possible for the higher efficiency model. Here, feedback has only a small effect. This shows that high efficiency models cannot be regulated by feedback to observe SFE at cloud-scales. This is a key result of this work. Furthermore, in both cases, increasing the feedback comes at the cost of shifting the virial parameter away from the observed values. This puts an additional constraint on feedback, as other cloud-scale parameters need to be considered when increasing the feedback strength to regulate SF.

4.7.2 Early radiative feedback

The eff1 model and eff001 model were run with RT enabled. This added a component to the feedback, increasing its strength in the first Myrs after SF. Radiative feedback only matters in the first few million years after the birth of a stellar population; later feedback is dominated by SNe, which occur from 4-40 Myr after SF Agertz et al. (2013). Figure 4.9 shows the effects of RT on various parameters for the eff001 model. RT has a similar effect on the eff1 model, which is shown in Appendix A. One can see that the surface density gets shifted towards lower densities, away from the observational distribution. However, there is only a minimal effect on the other parameters; most notably, enabling RT does not affect the SFE. This is surprising because it means that despite changing the surface density distribution, the clouds have the same properties and efficiencies as before. Early RT is therefore not able to lower

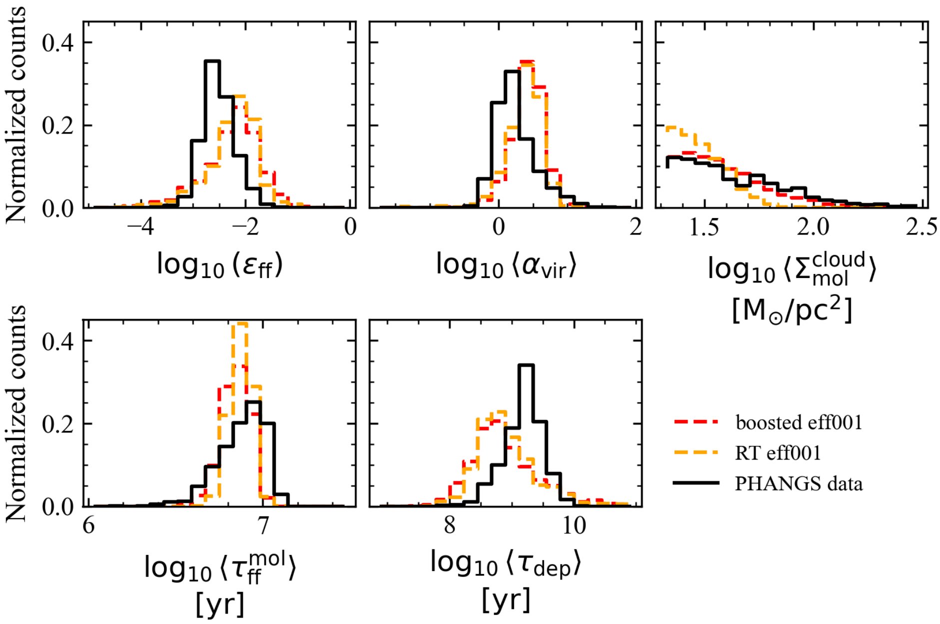

Figure 4.9: Effects of radiative transfer. All panels show the boosted eff001 model, once without radiative transfer (red) and once with (orange). The black line indicates the observational data from Leroy et al. (2025).

observed efficiencies. The underlying physics or RT are complex, and implementing them is not trivial. Different ways of implementing RT might cause slight differences in the response of the gas. Including a radiation field through RT will also have consequences on the formation and destruction of CO and H_2 (Glover & Clark, 2012). This is something that would need to be considered in future studies that track CO or H_2 directly, which is discussed further in Section 4.9.

4.8 Sensitivity to threshold parameters

For all simulations, the molecular hydrogen density was estimated by simple cuts to the number density $n_{\rm th}$ and the temperature $T_{\rm th}$ of the gas. The sensitivity to those cuts is shown in Figure 4.10 together with the cut for the stellar age included in SF calculations, for the boosted eff001 model. Both the cut for the stellar age and the temperature cut have minimal impact on the distribution of the various parameters. Here, it should be noted that the bottom middle three panels are independent of $t_\star$ and therefore show no variation. Varying $n_{\rm th}$ changes the distribution more noticeably, lowering $\epsilon_{\rm ff}$ for lower density cuts. This is expected as lower cuts mean that more gas, especially lower-density gas, is included in the analysis, causing lower SFE. This means that a more careful analysis by more accurately tracking molecular hydrogen will have the strongest effects if the selected density cut of $n_{\rm th} = 50\ {\rm cm}^{-3}$ is inaccurate, whereas there will only be very minor adjustments due to the temperature cuts. Furthermore, it does not matter much to what timescale SF is traced. However, this assumes no spatial decorrelation between the stellar tracers and SF events, something that appears in reality and needs to be included in more careful treatment (Hu et al., 2024).

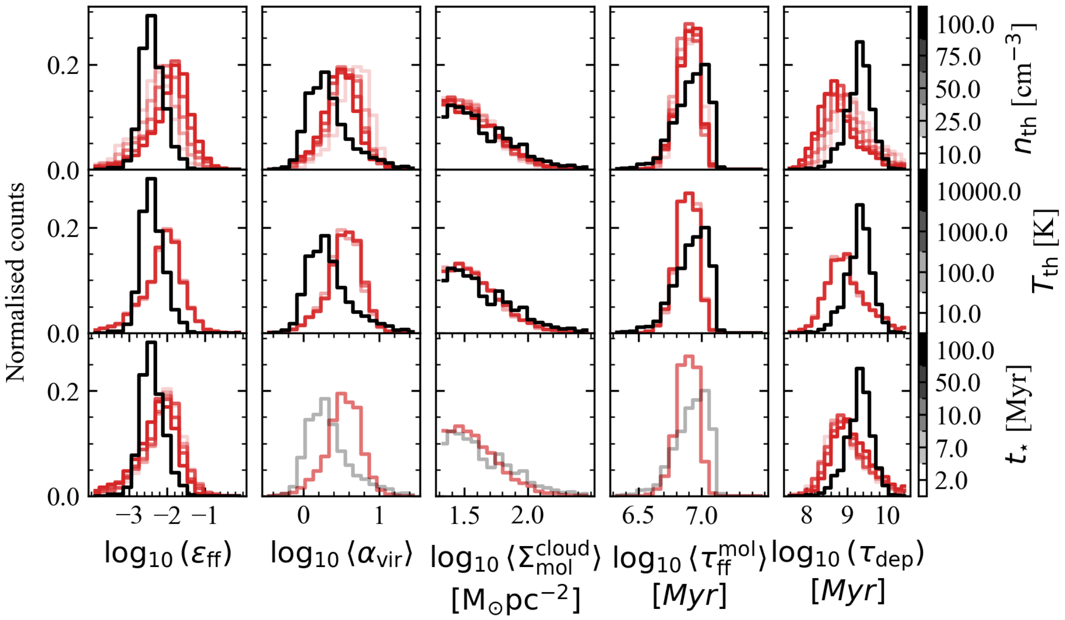

Figure 4.10: Sensitivity of observed efficiency to the threshold parameters n_{th}, T_{th} and $t_\star$. The rows show the sensitivity to the variation of the cuts $n_{\rm th}$, $T_{\rm th}$ and $t_\star$ from top to bottom, respectively. The opacity is increased for a larger threshold value as indicated by the bars to the side. The cuts which are not varied are kept constant at the respective values of $n_{th} = 50$ cm^{-3}, $T_{th} = 100$ K and $t_\star = 7$ Myr. The columns show the normalised distributions for the different parameters. The three greyed out panels in the bottom row indicate parameters that do not depend on $t_\star$. The black line is the observed data from Leroy et al. (2025).

4.9 Caveats and conclusions

Before summarising the main findings of this work, the caveats of the analysis should be stated again. As discussed above, the simulations are treating a single isolated galaxy with no magnetic effects. This is a simplified situation. Magnetic effects will change the density distribution and have a small dampening effect on SF (Federrath & Klessen, 2012). Another factor of uncertainty is our treatment of selecting molecular hydrogen. Since the simulations do not track it directly, the simple density cuts serve as an approximation. Even though varying those density cuts does not seem to affect the parameters much, there might be a more complex relation between those cuts. For an ideal comparison with the observations, the selection of molecular hydrogen should match the tracing of the observations. This is non-trivial as the observations are also subject to approximations when tracing molecular hydrogen (Leroy et al., 2025). Tracking CO or H_2 in simulations directly is also not a simple task. There are many different aspects that need to be considered for an accurate tracking, with uncertainties arising from the fact that the tracing of CO requires sub-grid models of the density distribution (Glover & Clark, 2012).

Finally, this work only studied the impact of star formation models and feedback processes at a fixed numerical resolution. To understand the degree to which our results are generic, a convergence study should be undertaken, which we leave for future work.

Despite the above caveats, the results presented above are indicative of the direction SF models should go in to reproduce observational data. The main findings are as follows:

1. Models with low input efficiencies of around a few per cent match both cloud scale properties and SFE better than models with higher input efficiencies. However, there is no direct correlation between input efficiency and observed efficiency.
2. Feedback is not able to reduce the observed local efficiencies down to observed values for

high input efficiency models. Furthermore, feedback decreases the match to cloud-scale properties for almost all models.

3. Feedback makes a large difference in global parameters such as global SFR and global gas distribution.
4. The analysis shows almost no sensitivity to the introduced thresholds T_{th} and $t_\star$ and a small sensitivity to n_{th}.

Keeping the limits of this work in mind, these findings allow us to rule out certain high-efficiency models. The observation that low-efficiency models match observations better indicates that GMCs are intrinsically inefficient at forming stars, and it is not feedback that reduces the efficiency.

There are subtle differences between the low efficiency models, and the strength of the feedback needs to be carefully chosen if global parameters such as global SFR or global gas distributions, as shown in Figure 4.1, are of importance. However, even simple models such as the eff001 model and the PN model produce results that match the observations.

This work also highlights the need to study both the local and the global scales when evaluating SF models, seeing differences in how the various models compare at different scales. Furthermore, it should be noted that a surprising insight is that the PHANGS-ALMA data cannot resolve certain global differences. Inspecting the visual comparison of the various models, Figure 4.1 and Figure A.2, one can see that, for example, the PN model produces very different distributions of gas depending on the feedback strength. However, at the resolution of the study done by Leroy et al. (2025), the cloud-scale parameters remain largely unaffected.

Chapter 5

Outlook

The main aim of this thesis was to find which types of models can match the low observed SFE. It has been found that to reproduce these SFEs the input efficiencies of the models need to be low. The best matches are found in the boosted PN model, decalibrated FK model and eff001 model. It could also be shown that the feedback has only a small effect on local properties.

A natural next step would be to rerun the simulations, including a radiative field and tracking CO directly. This would allow for an even more direct comparison to the PHANGS-ALMA data using the conversion factor found by Leroy et al. (2025). Furthermore, clouds could be tracked to investigate the mass distribution and scaling relation of GMCs with different models similar to the work of Grisdale et al. (2018). Including magnetic effects in the simulations is another parameter that can be investigated. Finally, this analysis can be easily extended to investigate other SF models and compare them to different observational data.

Understanding which SF models to use is key in many studies using simulations on a galactic scale. As shown in this work, different models lead to different evolutions and properties of the galaxy, something that needs to be taken into account when modelling the evolution of galaxies.

Acknowledgements

I would like to thank my supervisor, Oscar Agertz, for the help and supervision during the duration of the project and for the support and opportunities beyond. I also thank the Galaxy group at the division for welcoming us bachelor students so openly and giving us a space to share progress and learn. Furthermore, I am grateful for my colleagues and friends who supported me during the writing of my thesis and were always there to aid me if needed. Finally, I would want to thank my girlfriend and family for enduring phases of stress and supporting me.

Acknowledgement of the use of AI

Large language models (i.e. Claude.ai and ChatGPT) have been used for this work as a support for coding, mainly in the generation of plotting code and functions to handle different data formats to reduce storage space. They were also used to check and review code. The code that handled the analysis and implemented the mathematics and physics was written without AI support.

During the writing of the thesis, Grammarly and the Overleaf spellchecker were used, both of which are AI-assisted.

References

Agertz, O., & Kravtsov, A. V. 2015, The Astrophysical Journal, 804, 18, doi: 10.1088/0004-637X/804/1/18

Agertz, O., Kravtsov, A. V., Leitner, S. N., & Gnedin, N. Y. 2013, The Astrophysical Journal, 770, 25, doi: 10.1088/0004-637X/770/1/25

Agertz, O., Pontzen, A., Read, J. I., et al. 2020, Monthly Notices of the Royal Astronomical Society, 491, 1656, doi: 10.1093/mnras/stz3053

Behroozi, P. S., Wechsler, R. H., & Conroy, C. 2013, The Astrophysical Journal, 770, 57, doi: 10.1088/0004-637X/770/1/57

Belfiore, F., Leroy, A. K., Williams, T. G., et al. 2023, Astronomy and Astrophysics, 678, A129, doi: 10.1051/0004-6361/202347175

Chabrier, G. 2003, Publications of the Astronomical Society of the Pacific, 115, 763, doi: 10.1086/376392

Ejdetjärn, T., Agertz, O., Östlin, G., Renaud, F., & Romeo, A. B. 2022, Monthly Notices of the Royal Astronomical Society, 514, 480, doi: 10.1093/mnras/stac1414

Federrath, C., & Klessen, R. S. 2012, The Astrophysical Journal, 761, 156, doi: 10.1088/0004-637X/761/2/156

Glover, S. C. O., & Clark, P. C. 2012, Monthly Notices of the Royal Astronomical Society, 421, 116, doi: 10.1111/j.1365-2966.2011.20260.x

Grisdale, K., Agertz, O., Renaud, F., & Romeo, A. B. 2018, Monthly Notices of the Royal Astronomical Society, 479, 3167, doi: 10.1093/mnras/sty1595

Grisdale, K., Agertz, O., Renaud, F., et al. 2019, Monthly Notices of the Royal Astronomical Society, 486, 5482, doi: 10.1093/mnras/stz1201

Hopkins, P. F., Narayanan, D., & Murray, N. 2013, Monthly Notices of the Royal Astronomical Society, 432, 2647, doi: 10.1093/mnras/stt723

Hopkins, P. F., Quataert, E., & Murray, N. 2011, Monthly Notices of the Royal Astronomical Society, 417, 950, doi: 10.1111/j.1365-2966.2011.19306.x

Hu, Z., Wibking, B. D., Krumholz, M. R., & Federrath, C. 2024, Monthly Notices of the Royal Astronomical Society, 534, 2426, doi: 10.1093/mnras/stae2241

Kennicutt, Jr., R. C. 1998, Annual Review of Astronomy and Astrophysics, 36, 189, doi: 10.1146/annurev.astro.36.1.189

Khokhlov, A. M. 1998, Journal of Computational Physics, 143, 519

Kim, J.-h., Abel, T., Agertz, O., et al. 2014, The Astrophysical Journal Supplement Series, 210, 14, doi: 10.1088/0067-0049/210/1/14

Kim, J.-h., Agertz, O., Teyssier, R., et al. 2016, The Astrophysical Journal, 833, 202, doi: 10.3847/1538-4357/833/2/202

Kretschmer, M., & Teyssier, R. 2020, Monthly Notices of the Royal Astronomical Society, 492, 1385, doi: 10.1093/mnras/stz3495

Krumholz, M. R., & McKee, C. F. 2005, The Astrophysical Journal, 630, 250, doi: 10.1086/431734

Leroy, A. K., Sun, J., Meidt, S., et al. 2025, The Astrophysical Journal, 985, 14, doi: 10.3847/1538-4357/adbcab

Licquia, T. C., & Newman, J. A. 2015, The Astrophysical Journal, 806, 96, doi: 10.1088/0004-637X/806/1/96

Moster, B. P., Naab, T., & White, S. D. M. 2013, Monthly Notices of the Royal Astronomical Society, 428, 3121, doi: 10.1093/mnras/sts261

Murray, N., & Rahman, M. 2010, The Astrophysical Journal, 709, 424, doi: 10.1088/0004-637X/709/1/424

Myers, P. C., Dame, T. M., Thaddeus, P., et al. 1986, Astrophysical Journal, 301, 398, doi: 10.1086/163909

Naab, T., & Ostriker, J. P. 2017, Annual Review of Astronomy and Astrophysics, 55, 59, doi: https://doi.org/10.1146/annurev-astro-081913-040019

NASA/ESA/CSA/STScI. 2023, PHANGS image mosaic, Image. https://www.esa.int/ESA_Multimedia/Images/2024/01/PHANGS_image_mosaic

Padoan, P., Haugbølle, T., & Nordlund, Å. 2012, The Astrophysical Journal, 759, L27, doi: 10.1088/2041-8205/759/2/l27

Padoan, P., Pan, L., Haugbølle, T., & Nordlund, Å. 2016, The Astrophysical Journal, 822, 11, doi: 10.3847/0004-637X/822/1/11

Rosolowsky, E., Hughes, A., Leroy, A. K., et al. 2021, Monthly Notices of the Royal Astronomical Society, 502, 1218, doi: 10.1093/mnras/stab085

Semenov, V. A., Kravtsov, A. V., & Gnedin, N. Y. 2016, The Astrophysical Journal, 826, 200, doi: 10.3847/0004-637X/826/2/200

Soler, J. D., Zari, E., Elia, D., et al. 2023, Astronomy and Astrophysics, 678, A95, doi: 10.1051/0004-6361/202347608

Springel, V. 2010, Monthly Notices of the Royal Astronomical Society, 401, 791, doi: 10.1111/j.1365-2966.2009.15715.x

Sun, J., Leroy, A. K., Rosolowsky, E., et al. 2022, The Astronomical Journal, 164, 43, doi: 10.3847/1538-3881/ac74bd

Teyssier, R. 2002, Astronomy and Astrophysics, 385, 337, doi: 10.1051/0004-6361:20011817

Whitaker, K. E., van Dokkum, P. G., Brammer, G., & Franx, M. 2012, The Astrophysical Journal Letters, 754, L29, doi: 10.1088/2041-8205/754/2/L29

Appendix A

Plots and Figures

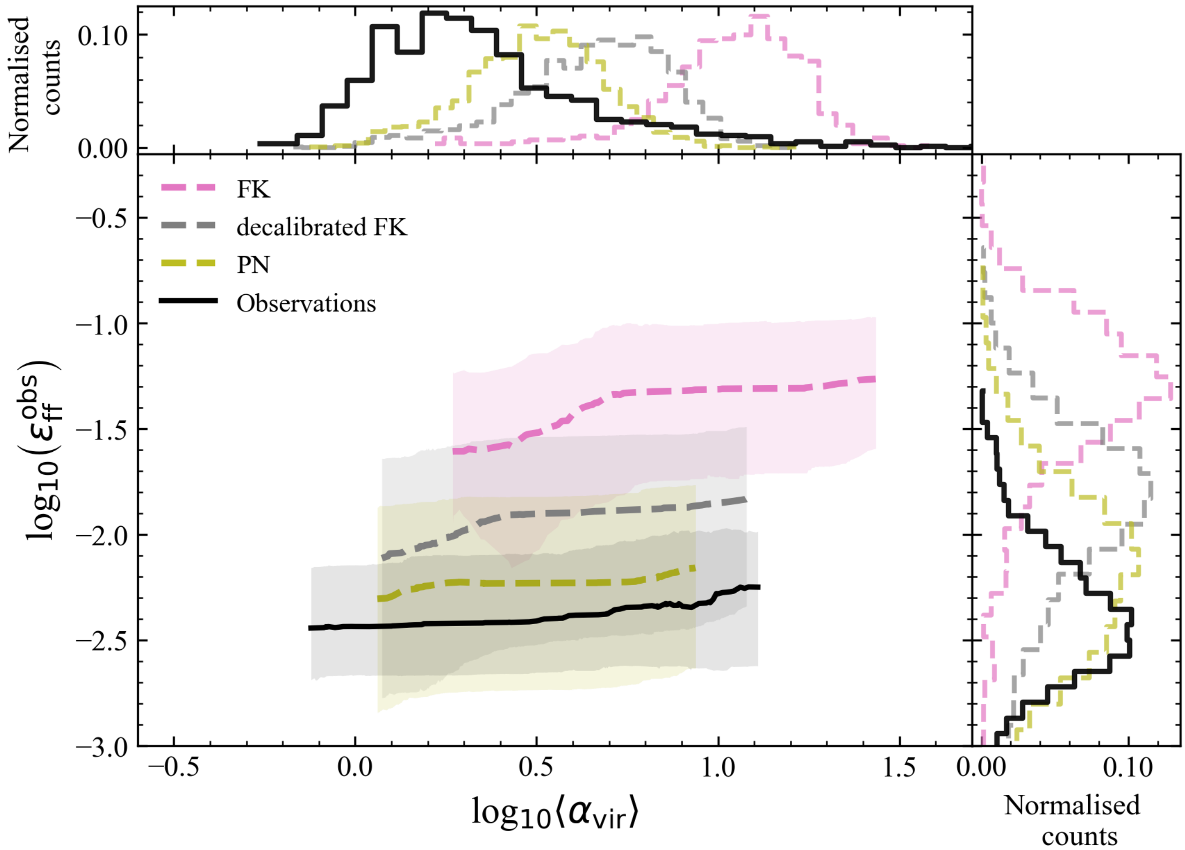

Figure A.1: Boosted FK model, decalibrated FK model and similar to Figure 4.6.

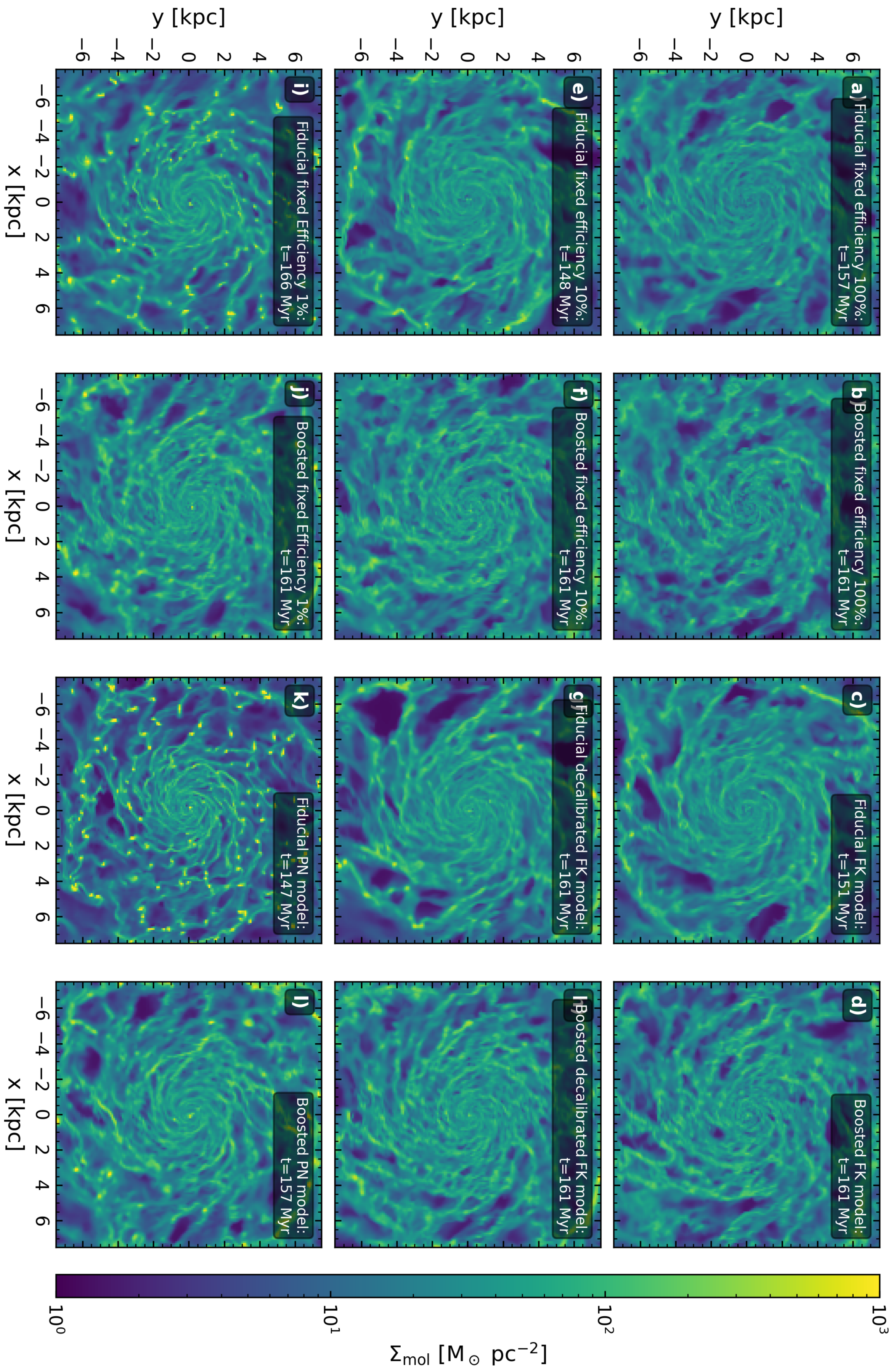

Figure A.2: Additional simulations to Figure 4.1.

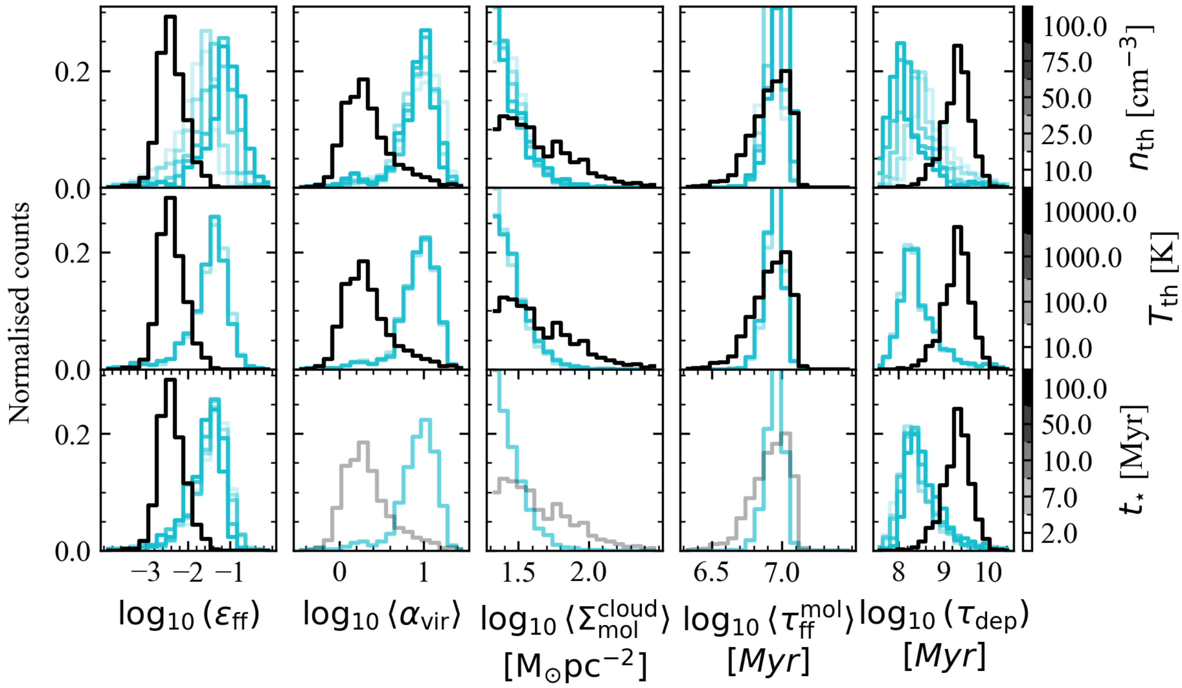

Figure A.3: Sensitivity to threshold parameters of the eff01 model similar to Figure 4.10.

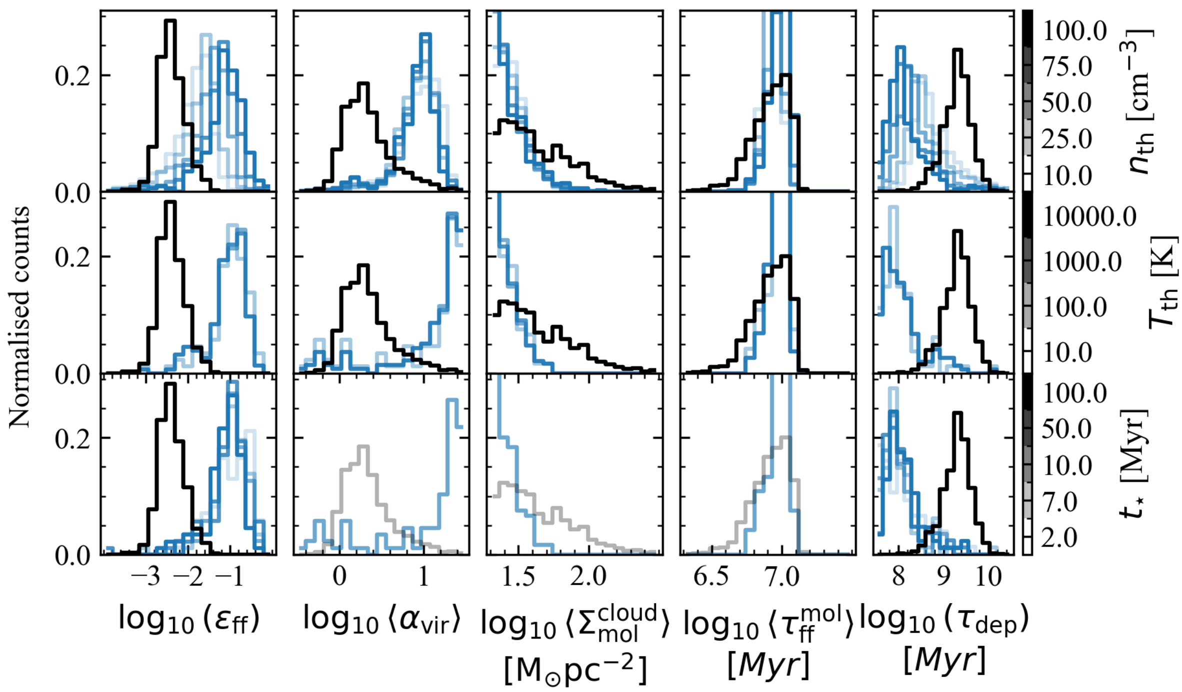

Figure A.4: Sensitivity to threshold parameters of the eff1 model similar to Figure 4.10.

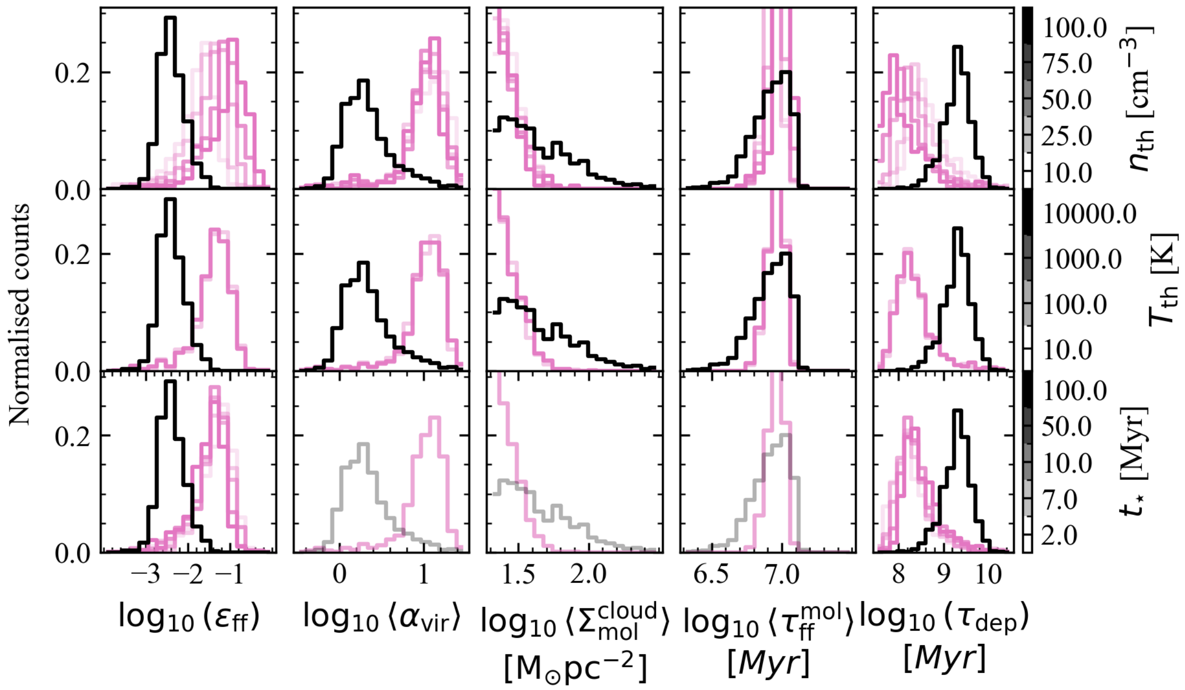

Figure A.5: Sensitivity to threshold parameters of the FK model similar to Figure 4.10.

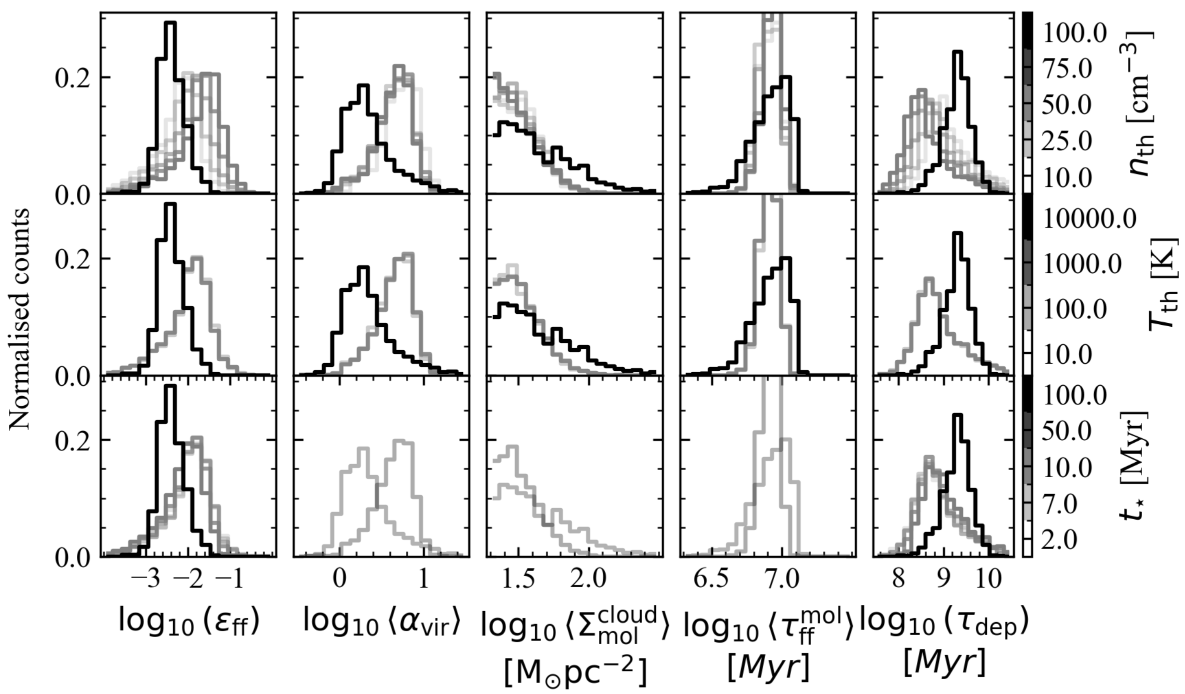

Figure A.6: Sensitivity to threshold parameters of the decalibrated FK model similar to Figure 4.10.

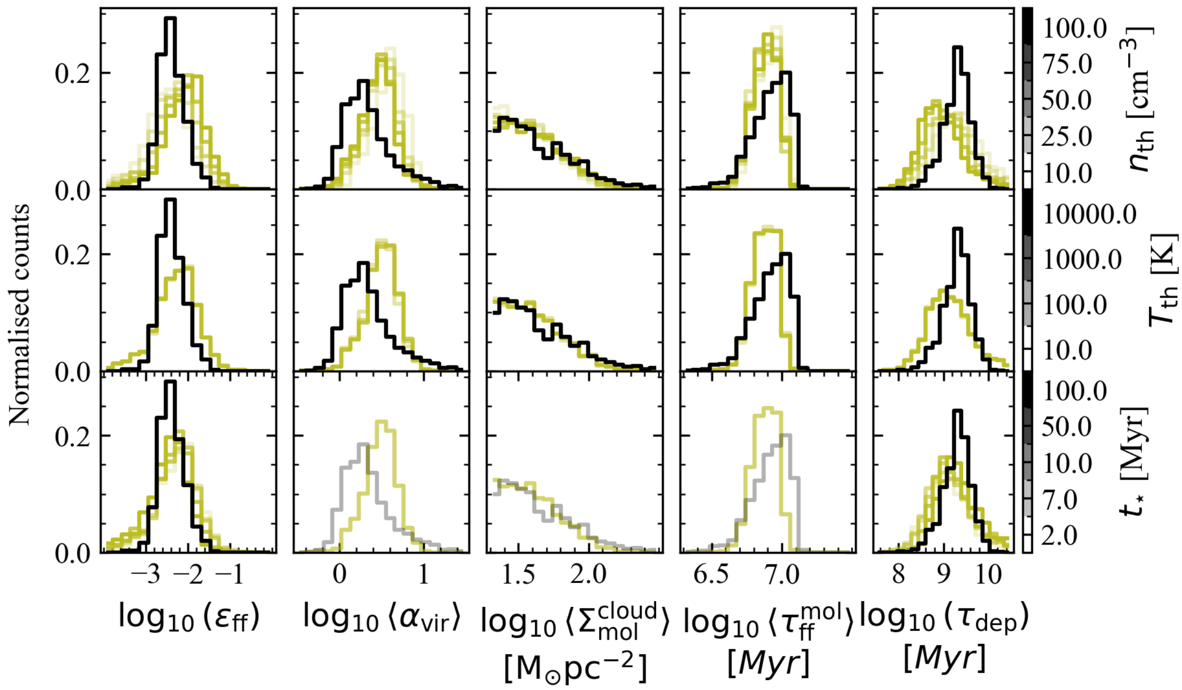

Figure A.7: Sensitivity to threshold parameters of the PN model similar to Figure 4.10.

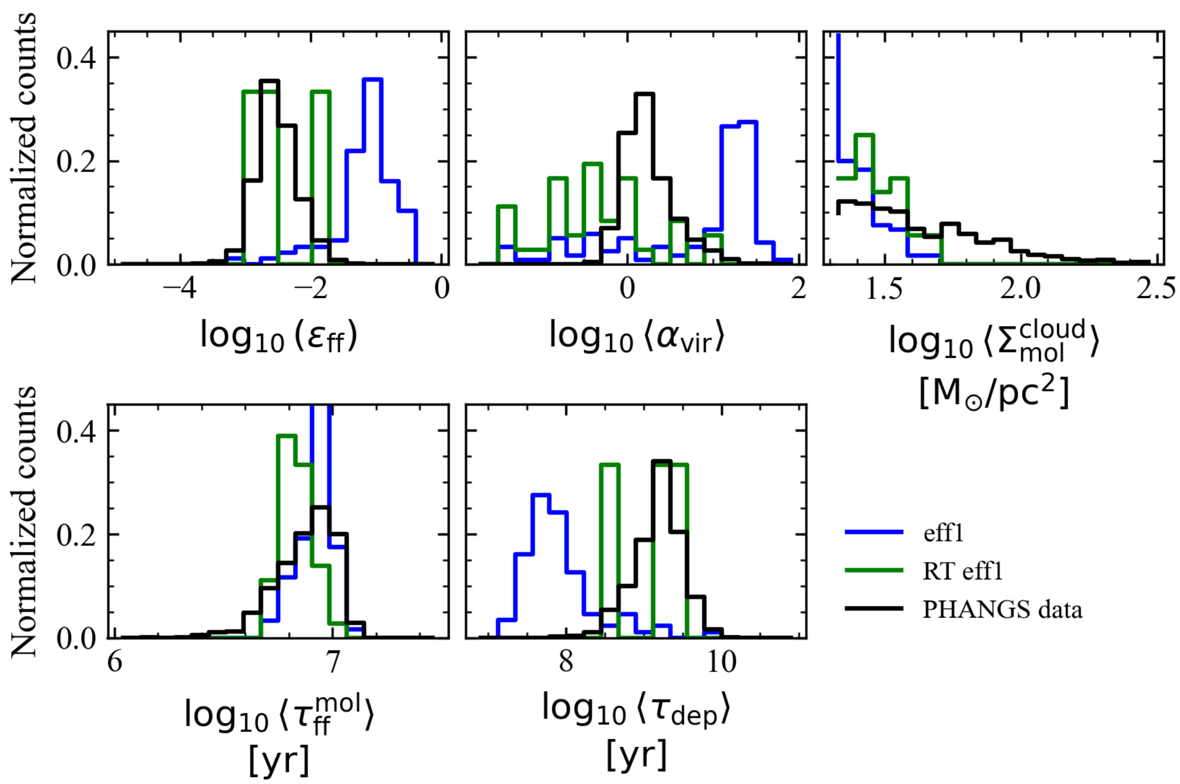

Figure A.8: Effects of RT on the eff1 model. It needs to be noted that due to the completeness cut $\Sigma_{\rm mol} > 20\ M_\odot$ only three data points are plotted in the top left and bottom right panels.